Investigation of Galactic open cluster remnants: the case of NGC 7193*

RAA 2017 Vol. **17** No. **1**, 4 (24pp) doi: 10.1088/1674–4527/17/1/4

http://www.raa-journal.org *http://iopscience.iop.org/raa*

***R**esearch in*
***A**stronomy and*
***A**strophysics*

Investigation of Galactic open cluster remnants: the case of NGC 7193 ⋆

Mateus de Souza Angelo[1], João Francisco Coelho dos Santos Jr[1], Wagner José Barbosa Corradi[1], Francisco Ferreira de Souza Maia[1] and Andrés Eduardo Piatti[2,3]

[1] Departamento de Física, ICEx, Universidade Federal de Minas Gerais, Av. Antônio Carlos 6627, 31270-901 Belo Horizonte, MG, Brazil; *altecc@fisica.ufmg.br*
[2] Observatorio Astronómico, Universidad Nacional de Córdoba, Laprida 854, 5000, Córdoba, Argentina
[3] Consejo Nacional de Investigaciones Científicas y Técnicas, Av. Rivadavia 1917, C1033AAJ, Buenos Aires, Argentina

Received 2016 May 24; accepted 2016 September 14

Abstract Galactic open clusters (OCs) that survive the early gas-expulsion phase are gradually destroyed over time by the action of disruptive dynamical processes. Their final evolutionary stages are characterized by a poorly populated concentration of stars called an open cluster remnant (OCR). This study is devoted to assessing the real physical nature of the OCR candidate NGC 7193. GMOS/Gemini spectroscopy of 53 stars in the inner target region were obtained to derive radial velocities and atmospheric parameters. We also employed photometric and proper motion data. The analysis method consists of the following steps: (i) analysis of the statistical resemblance between the cluster and a set of field samples with respect to the sequences defined in color-magnitude diagrams (CMDs); (ii) a 5-dimensional iterative exclusion routine was employed to identify outliers from kinematical and positional data; (iii) isochrone fitting to the $K_s \times (J - K_s)$ CMD of the remaining stars and the dispersion of spectral types along empirical sequences in the $(J - H) \times (H - K_s)$ diagram were checked. A group of stars was identified for which the mean heliocentric distance is compatible with that obtained via isochrone fitting and whose metallicities are compatible with each other. Fifteen of the member stars observed spectroscopically were identified together with another 19 probable members. Our results indicate that NGC 7193 is a genuine OCR, of a once very populous OC, for which the following parameters were derived: $d = 501 \pm 46$ pc, $t = 2.5 \pm 1.2$ Gyr, $\langle [\mathrm{Fe/H}] \rangle = -0.17 \pm 0.23$ and $E(B-V) = 0.05 \pm 0.05$. Its luminosity and mass functions show depletion of low mass stars, confirming the OCR is in a dynamically evolved state.

Key words: open cluster remnants — Galactic open clusters

1 INTRODUCTION

Galactic open clusters (OCs) gradually lose their stellar content as they evolve. Those that survive both the early gas-expulsion phase (first $\sim$ 3 Myr), during which the cluster is embedded in its progenitor molecular cloud, and the subsequent phase, when the cluster is largely gas free and its overall dynamics are dominated by stellar mass loss, enter into a long-term evolutionary phase. During this last phase, timescales for stellar mass loss through stellar evolution are considerably longer than dynamical timescales and purely dynamical processes dominate the evolution of the cluster. The interplay between internal forces (two-body or higher order interactions) and external ones (interactions with the Galactic tidal field, collisions with molecular clouds and/or disc shocking) contributes to the decrease of total mass in the clusters (Pavani et al. 2011, hereafter PKBM11; Pavani et al. 2001; Bica et al. 2001, hereafter BSDD01; Portegies Zwart et al. 2010).

Galactic open cluster remnants (OCRs) are the fossil residue of OCs evolution. These structures can be de-

⋆ Based on observations obtained at the Gemini Observatory, which is operated by the AURA under a cooperative agreement with the NSF on behalf of the Gemini partnership: NSF (United States), STFC (United Kingdom), NRC (Canada), CONICYT (Chile), ARC (Australia), CNPq (Brazil) and CONICET (Argentina).

fined as stellar aggregates in advanced stages of dynamical evolution and in the process of dissolution into the general Galactic disc field. OCRs are intrinsically poorly populated (typically consisting of a few tens of stars), but with enough members to show evolutionary sequences in color-magnitude diagrams (CMDs), as a result of the dynamical evolution of an initially more massive stellar system (PKBM11 and references therein).

Numerical simulations taking into account the effects of stellar evolution, the Galactic tidal field and realistic initial mass functions (de La Fuente Marcos 1998) showed that the initial number of stars in an OC is the main parameter determining its lifetime, for a given Galactocentric distance. The final stellar content of the remnant also depends on the initial mass function (MF) and on the fraction of primordial binaries. Depending on the mentioned parameters, OCs dissolve in $0.5 - 2.5$ Gyr (Portegies Zwart et al. 2001). These numerical simulations suggest that currently observable OCRs can be descendants of initially rich OCs, containing as many as $N_0 \sim 10^4$ members when they were born. At the solar circle, an OC that rich is expected to last several Gyr (de la Fuente Marcos et al. 2013). As a consequence of dynamical interactions (internal relaxation and the action of the Galactic tidal field), remnants are expected to be biased towards stable dynamical configurations (binaries and long-lived triples, de La Fuente Marcos 1998) and deficient in low mass stars, due to their preferential evaporation.

BSDD01 devised a method to search for possible open cluster remnants (POCRs) based on the comparison of star counts in the objects' inner areas with those in the surrounding field as well as with Galactic model predictions. For all of the 34 objects analyzed, there is a significant overdensity of stars in the POCRs regions. Although a density enhancement is a necessary condition for a system to be classified as an OCR, it is not a sufficient one. It is also known that a random distribution of field stars can mimic sequences of evolved OCs in photometric diagrams, as has been verified in the cases of, e.g., NGC 5385, NGC 2664, Collinder 21 (Villanova et al. 2004) and ESO 442-SC04 (Maia 2012). As OCRs are hardly distinguishable from field stars, a joint study involving different kinds of data (proper motions, radial velocities, spectroscopic and photometric information) and the analysis of their dispersion are necessary for the proper selection of their members and thus to discard such an enhancement as a chance alignment of stars.

NGC 7193 has an OCR appearance and it is currently classified as an OC in Dias et al.'s (2002, hereafter DAML02) catalog (version 3.4[1]). It is currently absent from the WEBDA[2] database. Since NGC 7193 is a high Galactic latitude object ($\ell = 70.1°$, $b = -34.3°$), it is not largely affected by interstellar dust in the Galactic disc and it is little contaminated by field stars. Compared to other confirmed OCRs, previously characterized by including spectroscopy beyond the more usual photometric and proper motion analyses (Ruprecht 3, Pavani et al. 2003; NGC 1252, de la Fuente Marcos et al. 2013; NGC 1901, Carraro et al. 2007), NGC 7193 is the most populous one.

Tadross (2011) performed a photometric analysis of 120 NGC OCs, including NGC 7193. For each target, photometric data in the near-infrared were extracted from 2MASS (Skrutskie et al. 2006) for stars in the cluster region and also for a comparison field. His analysis included redetermination of the cluster centers, construction of radial density profiles (RDPs) and determination of fundamental parameters (age, distance and interstellar reddening) by means of isochrone fitting on field-subtracted CMDs.

Our procedure, on the other hand, was based on a star-by-star verification of their properties for the selection of members. The present paper is intended to assess conclusively the physical nature of the OCR candidate NGC 7193. To accomplish this goal, we propose a method that combines photometric and spectroscopic information for this cluster for the first time. Our analysis includes the dispersions in the radial velocities, proper motions, spectral types and metallicities as measures of the physical connection between stars. This approach is critical in the cases of stellar systems containing a scanty number of stars.

This paper is organized as follows: We describe the collection and reduction of the observational material in Section 2. In Section 3 we present the methodology developed to verify the contrast between target and surrounding field with respect to star counts and to determine atmospheric parameters. Data analysis is presented in Section 4, which involves photometric, spectroscopic and proper motion information in order to assign stellar membership. Luminosity and MFs for NGC 7193 are derived in Section 5. In Section 6 we summarize the main conclusions.

2 DATA COLLECTION AND REDUCTION

Analysis of the physical nature of NGC 7193 relies on spectra obtained with the Gemini South (program IDs:

[1] *http://www.wilton.unifei.edu.br/ocdb/*
[2] *https://www.univie.ac.at/webda/*

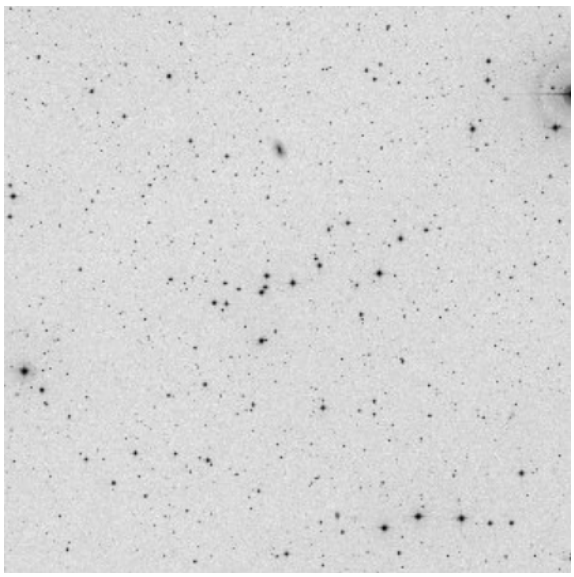

Fig. 1 Digitized Sky Survey (DSS2) red map of the NGC 7193 field. North is up, East on the left. The image is $30'$ on a side.

GS-2012B-Q-38, GS-2013-B-Q41 and GS-2014B-Q-71) telescope and complemented with near-infrared (JHK_s - bands) photometric data from 2MASS and proper motions from UCAC4 (Zacharias et al. 2013). VizieR[3] was used to extract data from both catalogs for stars within a circular region with radius equal to 1° centered on NGC 7193 coordinates $\mathrm{RA_{J2000}} = 22^\mathrm{h}\ 03^\mathrm{m}\ 03^\mathrm{s}$, $\mathrm{Dec_{J2000}} = 10^\circ\ 48'\ 06''$, provided by DAML02. This region is large enough to contain the whole field of NGC 7193 (Fig. 1). This search radius is about 10 times the apparent radius provided by DAML02. Entries containing extended source contamination flags were excluded. In addition, version 3.1 of ELODIE[4] (Moultaka et al. 2004) and PHOENIX[5] (Husser et al. 2013) libraries of stellar spectra were also employed.

2.1 Gemini GMOS Spectroscopic Data

Spectra of 53 selected stars distributed in three $5.5 \times 5.5\,\mathrm{arcmin}^2$ regions in the NGC 7193 field were collected with the Gemini South (proposal GS-2013-B-Q41) multi-object spectrograph (GMOS-S) in MOS observing mode. Slitlets were cut in five masks guided by the star positions defined in the u filter ($\lambda_{\mathrm{eff}} = 350\,\mathrm{nm}$) images taken previously. The spectra were obtained with the grating B1200_G5321 and with slit widths of $1.0''$, covering the spectral range $3835 - 5425\,\text{Å}$ with a resolution of $R \approx 2000$. For each mask, spectra were obtained in two central wavelengths (λ_c), in order to correct for CCDs gaps. We took several relatively short exposures in order to avoid saturating the detectors. One standard star (HD 211341) from the list of Casagrande et al. (2011) was also observed in longlist mode. Two other standards (HD 68089 and HD 38254) from the same list were observed with the same instrumental setup during two other observing runs (proposals GS-2012B-Q-38 and GS-2014B-Q-71). Typical seeing was about $1.0''$ for all observing nights. The observation log is detailed in Table 1. The number of repeated exposures with the same integration time are indicated in parentheses.

Table 1 Log of Spectroscopic Observations

Object	α_{2000} (h: m: s)	δ_{2000} (°: ′: ″)	λ_c (nm)	Mask #	Exposure (s)
		2013 Jan 03			
HD 68089	08:09:05	–42:04:28			
			455	longslit	20 (2)
			460	longslit	20 (2)
		2013 Sep 08			
NGC 7193W	22:02:49	10:49:17			
			458	5	100 (3)
			463	5	100 (3)
			458	6	100 (3)
			463	6	100 (3)
HD 211341	22:16:06	16:01:15	458	longslit	10 (2)
			463	longslit	10 (2)
		2013 Nov 03			
NGC 7193E	22:03:09	10:46:38			
			458	3	100 (3)
			463	3	100 (3)
			458	4	100 (3)
			463	4	100 (3)
		2013 Nov 06			
NGC 7193SW	22:02:48	10:43:22			
			458	8	100 (3)
			463	8	100 (3)
		2015 Jan 22			
HD 38254	05:42:51	–35:06:10			
			458	longslit	40 (2)
			463	longslit	40 (2)

Data reduction was carried out using IRAF[6] standard routines from the GEMINI package. Images were bias and flat field corrected. Bad pixel masks were used to interpolate across defective regions of the CCDs and

[3] *http://vizier.u-strasbg.fr/viz-bin/VizieR*

[4] *http://www.obs.u-bordeaux1.fr/m2a/soubiran/download.html*

[5] *http://phoenix.astro.physik.uni-goettingen.de/*

[6] IRAF is distributed by the National Optical Astronomy Observatory, which is operated by the Association of Universities for Research in Astronomy (AURA) under cooperative agreement with the National Science Foundation.

cosmic rays were removed. Twilight flats were obtained for each GMOS mask and reduced in order to correct for illumination gradients along the slits. Wavelength calibrations were performed by fitting $6^{\rm th}$-order Chebyshev polynomials to the positions of lines identified in CuAr arc lamp spectra. The root mean square (rms) values of the wavelength solutions were typically 0.15 Å. These solutions were used to rectify the 2D spectra, which were separated in different image extensions, sky subtracted and then collapsed to 1D spectra. For each star, spectra taken at the same $\lambda_{\rm c}$ were summed to increase the signal to noise ratio (S/N). After that, spectra taken at different $\lambda_{\rm c}$ were combined to get the full wavelength range. Because the GMOS observations were not performed at the parallactic angle, all science spectra were normalized to the pseudo-continuum by fitting low-order polynomials (typically 9 or 10 cubic splines along the whole wavelength range) to the flux upper envelope. The IRAF task *continuum* was employed in this step.

3 THE METHOD

3.1 Radial Density Profile and Limiting Radius Determination

In order to construct the RDP of NGC 7193 and analyze its central stellar overdensity with respect to the background, a tentative redetermination of central coordinates was performed. In this step, the sample of stars was restricted to the following magnitude limits: 15.8, 15.1 and 14.3 mag at J, H and K_s, respectively. These limits ensure both data completeness larger than 99 per cent and good photometric quality (S/N > 10)[7]. We did not use the spatial density profiles in RA and DEC to determine the cluster center because of the scarcity of stars. The central coordinates provided in DAML02 were adopted as a first guess in order to construct the RDP of NGC 7193 and analyze its central stellar overdensity with respect to the background. Next, we manually varied these coordinates within $\sim 1.5'$ from the original ones. For each center, an RDP was constructed by counting the number of stars inside circular rings whose widths varied from $0.75'$ to $2.0'$, in steps of $0.25'$, and divided this number by the respective ring area. We looked for central coordinates which resulted in an RDP with the highest central stellar overdensity compared to the mean background density. The narrower rings are ideal to probe the central regions due to their larger stellar densities, while the wider ones are better to probe the external regions. This prevents either region of the cluster from being undersampled (Maia et al. 2010, hereafter MSC10).

The central coordinates ($\rm RA_{J2000}$, $\rm DEC_{J2000}$) = ($22^{\rm h}\ 03^{\rm m}\ 08^{\rm s}, 10^{\circ}\ 48'\ 14''$) were adopted ($1.2'$ away from the center given in literature). The NGC 7193 RDP is shown in Figure 2. The inset in Figure 2 shows the region selected for estimation of the mean background density, $\sigma_{\rm bg} = 0.31$ stars arcmin^{-2} (continuous line) and its 1σ uncertainty, $\Delta\sigma_{\rm bg} = 0.04$ stars arcmin^{-2} (dotted lines). Densities tend to fluctuate around the $\sigma_{\rm bg}$ value starting from $R \approx 10'$, which we adopted as the cluster's limiting radius ($R_{\rm lim}$). Density profile models (e.g., King 1962) were not fitted to NGC 7193 RDP, since the scarcity of stars, field fluctuations and asymmetries in the stellar spatial distribution increase the uncertainties associated with the derived structural parameters, like core and tidal radii, precluding a statistically significant fit.

Although the NGC 7193 RDP shows a central stellar overdensity compared to the background, which is the first step in order to establish the physical nature of a stellar aggregate (BSDD01), it is useful to evaluate, with a statistical method, the contrast between the number of stars counted in the inner regions of the cluster and that in a set of samples chosen around the target field for different $R_{\rm lim}$. We devised an algorithm that follows the prescriptions detailed in PKBM11. The method consists of randomly selecting a set of circular field samples inside the extraction region centered on the OCR coordinates. Figure 3 shows an example of neighboring field samples (with radius $10'$ in Fig. 3) randomly selected around NGC 7193. The number of samples depends on their radii and varies from 1000 (for $R_{\rm lim} = 1'$) to 100 (for $R_{\rm lim} \geq 6'$).

For each test radius, the distribution of $N_{\rm field}/\langle N_{\rm field}\rangle$ values was built, where $N_{\rm field}$ is the number of stars counted within each field sample and $\langle N_{\rm field}\rangle$ is the average taken over the whole ensemble. Analogously, the ratio $N_{\rm OCR}/\langle N_{\rm field}\rangle$ was calculated, where $N_{\rm OCR}$ is the number of stars counted in the central region, represented as black filled circles within $10'$ of the central coordinates in Figure 3. The percentile corresponding to this ratio within the $N_{\rm field}/\langle N_{\rm field}\rangle$ distribution was also determined, for a given $R_{\rm lim}$. Fluctuations around each test radius were taken into account by repeating this procedure ten times.

Figure 4 shows the average percentiles and their associated 1σ uncertainties for each $R_{\rm lim}$. In the range $2 \leq R_{\rm lim}$ (arcmin) ≤ 6, the percentiles corresponding to the ratio $N_{\rm OCR}/\langle N_{\rm field}\rangle$ achieve values below 90% due to fluctuations in the concentration of stars across the cluster region. These fluctuations result in density val-

[7] *http://www.ipac.caltech.edu/2mass/overview/about2mass.html*

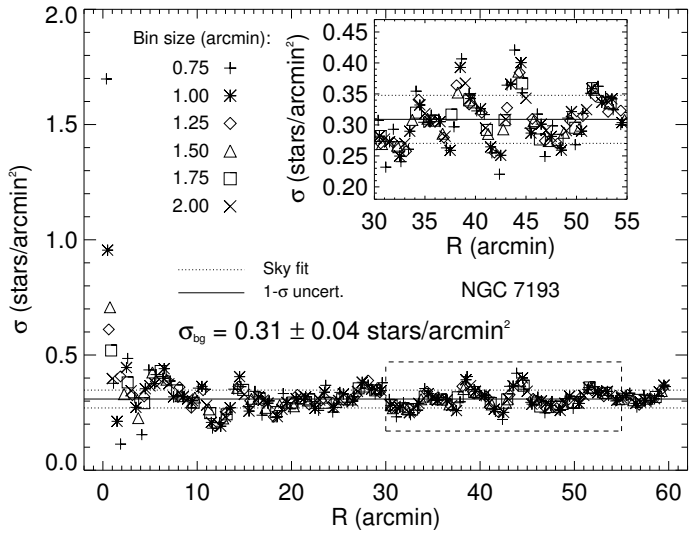

Fig. 2 RDP of NGC 7193. Different bin sizes are overplotted. The inset shows the region (*dashed rectangle*) selected for estimation of the mean background density ($\sigma_{\rm bg}$, *continuous line*) and its 1σ uncertainty (*dotted lines*).

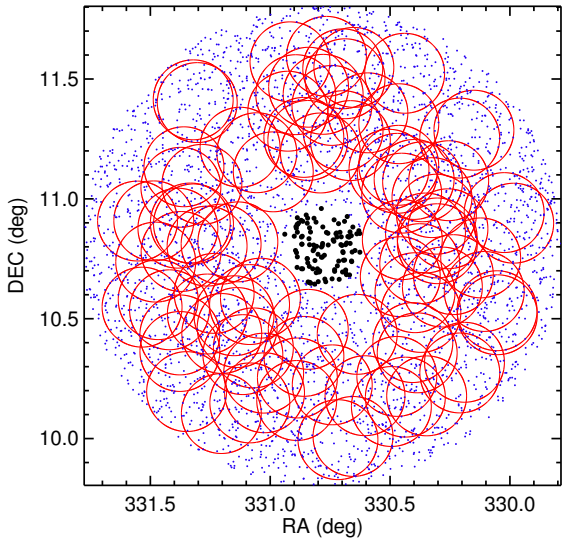

Fig. 3 Sky map of NGC 7193. Stars with $J \leq 15.8$, $H \leq 15.1$, $K_s \leq 14.3$ mag which are located within 1° of the central coordinates are shown. *Black circles* represent stars within $10'$. Other stars are plotted as *blue dots*. *Red circles* illustrate a set of 100 randomly selected field samples with radii equal to $10'$.

ues below $\sigma_{\rm bg}$ in this radius interval (Fig. 2). NGC 7193 shows a greater contrast in comparison to its field with respect to star counts for $R_{\rm lim}$ values between $7' - 11'$ (Fig. 4). The percentile for $R_{\rm lim} = 10'$ is slightly below 90%, but is still compatible with this value taking into account the uncertainty. In addition, all probable member stars are found (Sect. 4.4) within this limiting radius. For $R_{\rm lim} > 11'$, the percentiles are systematically below 90%, due to increasing field contamination.

The limiting radius of NGC 7193 can be converted to $R_{\rm lim} = 1.46$ pc at $\log(t/{\rm yr}) = 9.4$ by adopting a distance modulus of $(m - M)_0 = 8.5$ mag (Sect. 4.4). This result is quite consistent with the temporal evolution of the core radius values as shown in figure 2 of de La Fuente Marcos (1998), who performed an $N-$body simulation of a cluster with an initial population of $N_0 = 10^4$ stars which contained primordial binaries. This is an expected result, since in the far future, initially massive open clusters will leave behind only a core, with most of their stellar content dispersed into the background (Bonatto et al. 2004b; de La Fuente Marcos 1996).

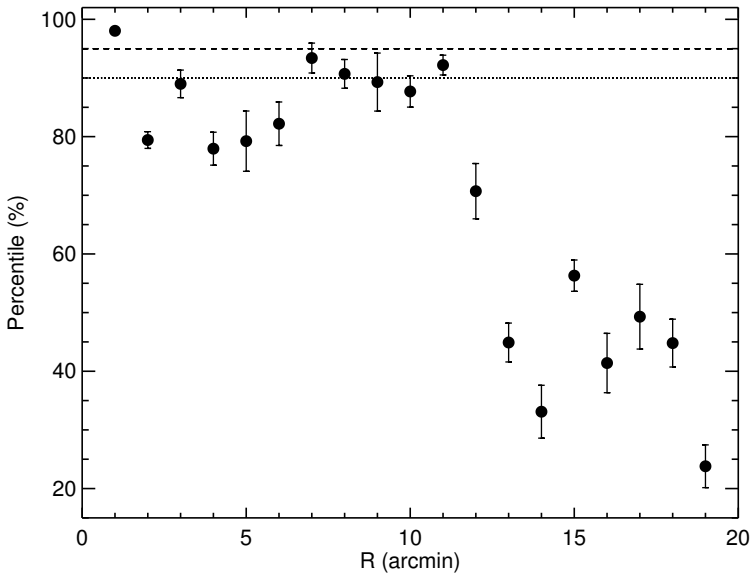

Fig. 4 Average percentiles and associated 1σ uncertainties corresponding to the ratio $N_{\rm OCR}/\langle N_{\rm field}\rangle$ within the $N_{\rm field}/\langle N_{\rm field}\rangle$ distribution for each test radius. Dotted and dashed lines mark the $90^{\rm th}$ and $95^{\rm th}$ percentiles respectively.

3.2 Spectroscopy: Atmospheric Parameter and Radial Velocity Determination

3.2.1 The cross-correlation method: ELODIE and PHOENIX spectral libraries

For determination of effective temperatures ($T_{\rm eff}$), logarithm of surface gravities, ($\log(g)$), metallicities ([Fe/H]) and radial velocities ($V_{\rm r}$), the spectra of our program stars were cross-correlated with stellar spectral templates obtained from the spectral libraries ELODIE and PHOENIX. The former is an empirical library containing 1962 spectra of 1388 stars covering the wavelength range $3900-6800$ Å and providing a large sampling in effective temperature ($3000 \leq T_{\rm eff}$ (K) $\leq 60\,000$). The latter is a synthetic library containing 27 704 spectra covering the wavelength range $500-55\,000$ Å and providing a better sampling in surface gravity ($0.0 \leq \log(g) \leq 6.0$) and metallicity ($-4.0 \leq$ [Fe/H] $\leq +1.0$) compared to ELODIE, although with a smaller coverage in $T_{\rm eff}$ ($\leq$ 12 000 K), since PHOENIX models assume local thermodynamic equilibrium. The sampling of the parameter space within the PHOENIX library has the following step sizes between models: $\Delta T_{\rm eff} = 100$ K for $T_{\rm eff}$ in the range 2300−7000 K and $\Delta T_{\rm eff} = 200$ K for $T_{\rm eff}$ in the range 7000−12000 K; $\Delta \log(g) = 0.5$ dex for $\log(g)$; Δ[Fe/H] $= 1.0$ dex for [Fe/H] between -4.0 and -2.0 and Δ[Fe/H] $= 0.5$ dex for [Fe/H] between -2.0 and $+1.0$.

Spectra of both libraries were taken at resolution $R = 10\,000$ and were degraded to match the resolution of our science spectra. Also, the wavelength grid used for the synthetic spectra was converted from a logarithmic to a linear scale and transformed from vacuum ($\lambda_{\rm vac}$) to air wavelengths ($\lambda_{\rm air}$) according to the transformation equations taken from Ciddor (1996) and valid for $\lambda > 2000$ Å. Specific flux densities ($F_\lambda^{\rm vac} = \frac{dE_\lambda}{dt\ d\lambda_{\rm vac}\ d{\rm Area}}$) were also converted from vacuum to air values:

$$F_\lambda^{\rm air} = \frac{dE_\lambda}{dt\ d\lambda_{\rm air}\ d{\rm Area}} = F_\lambda^{\rm vac}\left(\frac{d\lambda_{\rm vac}}{d\lambda_{\rm air}}\right).$$

3.2.2 The cross-correlation method: validation

The IRAF FXCOR task was employed for the construction of the cross-correlation function (CCF) of each spectra object−template pair. This task implements the algorithm described in Tonry & Davis (1979, hereafter TD79). The degree of similarity between line profiles of both spectra is given by the CCF peak (h), whose maximum value is normalized to 1.0. For each CCF, the task also calculates the TDR ratio, which is defined as the ratio of the CCF peak (h) to the rms of the CCF antisymmetric component ($\sigma_{\rm a}$). Formally, TDR $= h/(\sqrt{2}\sigma_{\rm a})$. The higher the TDR value is, the more prominent the central CCF peak will be in comparison to other (spurious) peaks. It is also inversely proportional to the uncertainty in radial velocity of the object relative to the template (equation 24 of TD79). Therefore, it is related to uncertainties associated with matching the spectral lines.

In order to check the above statements, we took a PHOENIX synthetic spectrum representative of the Sun

($T_{\rm eff}$ = 5800 K, $\log(g)$ = 4.5, [Fe/H] = [α/Fe] = 0.0; see Fig. 5) and cross-correlated it with all PHOENIX spectra with the same surface gravity and metallicity but with other values of $T_{\rm eff}$. In each case, the corresponding CCF peak (h) was calculated and then the ensemble of values was plotted as a function of $T_{\rm eff}$, as shown in the top left plot of Figure 6. The color scale indicates the TDR value.

We then verified the sensitivity of h in terms of $\log(g)$ and [Fe/H] following an analogous procedure: we fixed two of the atmospheric parameters (either $T_{\rm eff}$ *and* [Fe/H] or $T_{\rm eff}$ *and* $\log(g)$) and let the other one act as a free parameter (in all comparisons we kept [α/Fe] = 0.0). The results are shown in the middle ($\log(g)$) and rightmost ([Fe/H]) plots in the upper panels of Figure 6. In all cases the h values reach their maximum around those expected parameters.

After that we added noise to the original solar synthetic spectrum in order to simulate spectra whose S/N values are typical of our science ones (see Table 2 and Sect. 4.3). Those that were degraded in S/N are plotted in Figure 5 as blue and orange lines and their S/N values are 36 and 18, respectively. The same procedures outlined above were then employed in order to verify the sensitivity of the h values under variations in the atmospheric parameters in the cases of poorer quality spectra. This is shown in the middle and lower panels of Figure 6. Again, the h values peak at the expected parameters in each plot.

As we degrade the S/N of the object spectrum, the TDRs can reach higher values even in cases of cross-correlation with templates whose parameters are significantly different from those of the object spectrum. This is particularly true in the h vs. $\log(g)$ plot shown in the lower panels of Figure 6. This is a consequence of the growing antisymmetry of the CCF around its central peak as poorer quality spectra are employed in the cross-correlation (see also figs. 8 to 13 of TD79). Therefore the CCF peak is a more robust indicator of the similarity between a pair of spectra than the TDR ratio.

3.2.3 The cross-correlation method: application

To estimate $T_{\rm eff}$, our science spectra were cross-correlated with all templates from the ELODIE library. The templates from the whole library were also previously continuum normalized. Again, for each spectrum the flux upper envelope was fitted by employing cubic spline pieces along the whole wavelength range. The IRAF task *continuum* was used in order to perform an automated and uniform normalization procedure. This is a necessary step before cross-correlation to avoid the potential mistake of fitting the wrong CCF peak (for example, a coincidental peak in the CCF created by continuum variations). The templates most similar to a given object spectrum were chosen by identifying those that resulted in the maximum value of CCF peak.

The spectral type of a given object was determined by summing over the TDR values of those templates with the same spectral type within the selected subsample. The one with the highest TDR sum was adopted as the final spectral type. The object $T_{\rm eff}$ and its uncertainty ($\sigma_{T_{\rm eff}}$) were computed according to the averaged value and standard deviation for the chosen templates, weighted by the TDRs.

To derive $\log(g)$ and [Fe/H], we firstly filtered the parameter space covered by the PHOENIX models, restricting it to those templates whose effective temperatures are within the interval $[T_{\rm eff} - \sigma_{T_{\rm eff}}, T_{\rm eff} + \sigma_{T_{\rm eff}}]$, as obtained in the previous step. After cross-correlating our object spectrum with this group of templates (for which an automated normalization procedure was employed as explained above), those that resulted in the maximum value of the CCF peak were selected and ranked in ascending order of the TDRs. A subsample composed of the most well correlated theoretical templates was selected (that is, the ones that resulted in the highest value of h and in the highest values of TDR) and their average values of $\log(g)$ and [Fe/H] were calculated, weighted by the TDRs. Again, the uncertainties are equal to the weighted standard deviation of these values. The number of templates in this subsample is such that the maximum admitted uncertainties in $\log(g)$ and [Fe/H] correspond to the step size of these parameters in the PHOENIX library.

Within this subsample of PHOENIX templates, the one with the highest correlation was used to derive the radial velocity of our object spectrum relative to the template by executing the FXCOR task in interactive mode and fitting the CCF central peak with a Gaussian. Thus we ensure that a synthetic template of spectral type similar or equal to that of the object has been used to obtain the object's radial velocity. Then the IRAF RVCORRECT task was employed to derive the corresponding heliocentric correction.

To test the method, the procedure outlined in this section was applied to the spectra of the standard stars HD 68089, HD 211341 and HD 38254 and the resulting atmospheric parameters were compared to those found in the literature (Casagrande et al. 2011 and Holmberg et al. 2009). In order to enlarge our sample and probe a wider range of parameters, the method was applied to six other

Table 2 Stellar Parameters for Stars Observed Spectroscopically

ID	α_{2000}	δ_{2000}	$(\frac{\mathrm{S}}{\mathrm{N}})^a$	$\mu_\alpha \cos\delta$	μ_δ	ST	M_J^*	$(J-K_s)_0^*$	V_r	T_eff	[Fe/H]	$\log(g)$	Memb.
	(h: m: s)	($^\circ$: $'$: $''$)		(mas yr^{-1})	(mas yr^{-1})		(mag)	(mag)	(km s^{-1})	(K)	(dex)	(dex)	(**)
2	22:03:08	10:48:50	51	–13.1±1.7	–24.6±1.9	K0	0.0	0.61	–42.6±5.6	4868±227	–0.30±0.26	2.83±0.37	NM
3	22:03:08	10:48:14	86	–13.6±2.7	–17.4±1.7	F8	1.6	0.31	–48.1±5.1	6075±100	–0.50±0.50	3.75±0.27	M
4	22:03:02	10:48:27	138	–37.2±1.3	–39.0±0.8	G2	4.2	0.45	–17.4±3.1	5922±227	0.01±0.18	4.64±0.47	NM
6	22:03:09	10:47:57	126	5.0±0.9	–6.2±1.6	F3	3.0	0.25	–13.1±3.5	7007±200	0.00±0.50	4.74±0.40	M
7	22:03:19	10:47:25	48	2.1±2.5	4.1±2.9	G5	–0.2	0.50	–35.4±5.4	5230±100	–0.18±0.24	3.08±0.43	NM
9	22:03:12	10:46:08	36	–4.3±4.4	–9.8±4.7	K5	8.6	0.78	5.6±4.7	4312±227	–0.43±0.42	5.38±0.23	NM
11^d	22:03:06	10:46:19	14	–2.7±4.5	–2.1±4.5	K1	5.1	0.66	–28.6±4.9	5250±150	0.00±0.50	4.87±0.48	NM
13	22:03:06	10:45:53	45	11.5±4.9	–4.3±5.2	K0	4.1	0.48	–5.4±6.8	5368±100	0.00±0.50	4.48±0.32	M
14	22:03:09	10:45:24	154	9.4±1.1	–3.5±0.8	F3	2.8	0.23	–24.7±5.0	7123±200	0.03±0.12	4.53±0.41	M
15^d	22:03:10	10:45:13	65	4.6±5.0	3.5±5.0	F5	3.1	0.28	8.3±4.3	6455±242	–0.25±0.26	4.34±0.34	NM
16	22:03:06	10:44:07	19	–3.5±13.9	3.6±10.8	G0	2.5	0.39	38.4±4.2	5802±142	–0.28±0.26	4.10±0.30	NM
18	22:03:15	10:44:34	40	–4.8±4.2	–30.4±4.7	G8	2.7	0.38	–49.1±3.5	5394±110	–0.50±0.50	4.00±0.50	NM
19	22:03:04	10:44:14	18	–3.3±5.7	–15.3±5.6	F8	2.7	0.34	–27.4±3.5	5978±100	–0.53±0.12	4.03±0.40	NM
20	22:03:16	10:48:27	24	–0.3±3.2	0.1±3.4	K0	–2.9	0.61	–83.1±9.1	4868±227	–0.47±0.21	2.09±0.43	NM
21	22:03:14	10:48:08	99	–18.4±2.5	11.3±3.2	G0	2.3	0.40	–19.5±5.0	5627±170	–0.26±0.25	3.88±0.42	M
22	22:03:17	10:47:02	45	11.7±3.8	–6.2±4.1	F8	1.1	0.31	–55.6±2.0	6046±166	–0.25±0.25	3.75±0.40	NM
23	22:03:16	10:47:22	49	35.3±2.4	–23.4±3.2	G5	2.6	0.43	–87.7±2.1	5533±173	–0.13±0.22	4.12±0.37	NM
24^d	22:03:08	10:45:25	65	23.9±12.9	5.8±12.9	G0	2.2	0.38	–25.0±3.7	5780±100	–0.75±0.25	3.81±0.38	NM
25	22:03:14	10:44:34	68	–14.1±5.0	–18.6±5.4	K2	2.6	0.47	–87.3±6.0	4936±100	–0.50±0.50	3.99±0.36	NM
27	22:02:58	10:47:33	48	3.6±5.4	–4.2±5.7	F8	2.9	0.38	–68.2±5.1	5970±100	–0.50±0.50	4.19±0.29	NM
29	22:02:47	10:46:48	45	1.9±1.9	–14.6±5.7	G1	1.2	0.35	–48.9±11.0	5805±227	0.00±0.50	3.62±0.23	NM
30	22:02:49	10:48:33	88	–3.6±4.3	–6.4±4.7	G4	2.2	0.40	–49.9±3.9	5601±227	–0.50±0.50	3.81±0.30	NM
31	22:02:48	10:48:20	40	0.2±2.6	–5.3±3.0	G8	2.2	0.42	–10.8±5.2	5599±100	–0.29±0.25	3.82±0.40	M
32	22:02:58	10:48:40	24	–18.7±18.2	–5.0±18.2	G0	2.9	0.35	–6.7±7.4	5811±100	–0.50±0.50	4.21±0.28	NM
33	22:02:56	10:49:23	51	29.5±2.0	6.7±2.1	G5	3.7	0.36	–23.8±3.8	6072±297	0.00±0.50	4.51±0.43	M
34	22:02:43	10:48:57	45	20.8±0.9	–43.1±1.0	G8	0.6	0.43	–44.7±7.0	5445±227	0.08±0.18	3.41±0.48	M
36	22:02:48	10:50:08	18	–15.3±17.9	0.4±18.0	G5	3.4	0.41	–33.1±3.9	5640±109	–0.29±0.26	4.32±0.25	NM
37	22:02:41	10:50:25	46	–3.7±4.6	–15.0±5.0	K2	2.9	0.58	–43.7±13.0	4744±185	–0.20±0.27	4.09±0.42	NM
38	22:02:42	10:50:35	45	–9.2±4.1	–11.3±4.7	K7	9.5	0.83	–6.6±7.4	4014±100	–0.33±0.37	5.35±0.25	NM
39	22:02:54	10:51:28	65	–22.2±4.3	21.7±4.8	K0	3.3	0.48	29.2±6.4	5348±100	–0.41±0.21	4.25±0.27	NM
40	22:02:39	10:50:47	52	–22.6±2.1	–7.2±1.5	G0	0.4	0.42	–14.0±2.7	5639±227	–0.50±0.50	3.28±0.26	M
41	22:02:50	10:51:38	56	–2.8±1.4	–14.1±1.9	F8	1.4	0.34	0.2±5.5	6010±140	–0.21±0.25	3.83±0.33	M
42	22:02:54	10:51:17	67	–5.8±5.8	–2.3±2.0	F8	1.5	0.30	–16.2±3.0	6081±119	–0.36±0.22	3.71±0.46	NM
43	22:02:40	10:48:51	80	8.5±4.7	–4.6±5.1	B5	0.9	0.34	–42.2±3.0	6083±227	–1.98±0.12	3.38±0.34	NM
44	22:02:49	10:50:29	51	–3.9±5.1	–6.9±5.7	G5	–1.3	0.49	–284.6±4.8	5310±148	–0.32±0.28	2.78±0.46	NM
45	22:02:57	10:49:44	60	27.8±4.0	–3.4±4.1	G5	4.6	0.52	–1.2±2.2	5666±100	–0.11±0.21	4.88±0.35	M
46	22:02:53	10:50:01	31	–3.3±5.6	–5.6±5.6	G5	2.6	0.37	–47.8±3.0	5857±211	0.05±0.16	4.16±0.49	NM
47	22:02:40	10:51:44	40	16.0±4.9	–20.2±5.2	G0	2.7	0.38	4.2±3.6	5733±100	–0.50±0.50	4.00±0.50	NM
48^d	22:02:43	10:45:53	28	–0.7±4.3	–5.5±4.3	K2	5.5	0.74	44.4±4.8	5040±100	–0.19±0.25	4.87±0.38	NM
49	22:02:46	10:44:41	48	–20.7±4.4	–3.8±4.8	K3	$-^b$	0.61^c	15.6±9.7	4599±102	–	–	M
50^d	22:02:40	10:44:34	17	13.5±4.5	–8.6±4.5	K2	5.1	0.60	23.2±4.4	4999±130	–0.50±0.50	4.65±0.28	NM
51	22:02:39	10:44:27	90	85.8±6.4	–67.9±6.1	G5	3.3	0.43	24.1±2.2	5641±139	–0.50±0.50	4.27±0.29	NM
52^d	22:02:45	10:43:59	21	2.6±4.1	4.0±4.1	G8	3.4	0.48	–79.1±5.7	5294±100	–0.72±0.26	4.27±0.32	NM

Notes:

[a] At 4630 Å.

[b] We adopted $M_{K_s} = 4.1$ (assuming a K3V star), from SK: (1982) and Koornneef (1983) tables. The latter were transformed to 2MASS system according to the relations of Carpenter (2001).

[c] From Straižys & Lazauskaitė (2009) tables.

[d] Proper motions from the PPMXL (Roeser et al. 2010).

[e] For this star, $K_\mathrm{s} = 17.088, (J-K_\mathrm{s}) = -0.635$.

[*] From PARSEC isochrones (see details in the text).

[**] M means a member and NM means a non-member star.

Table 2 — *Continued.*

ID	α_{2000} (h: m: s)	δ_{2000} (°: ′: ″)	$(\frac{S}{N})^a$	$\mu_\alpha \cos\delta$ (mas yr^{-1})	μ_δ (mas yr^{-1})	ST	M_J^* (mag)	$(J-K_s)_0^*$ (mag)	V_r (km s^{-1})	$T_{\rm eff}$ (K)	[Fe/H] (dex)	log(g) (dex)	Memb. (**)
53[d]	22:02:38	10:44:18	46	52.5±12.9	–75.8±12.9	K0	5.0	0.62	–42.6±3.4	5358±100	–0.09±0.20	4.99±0.41	M
54[d,e]	22:02:52	10:43:32	28	1.3±5.4	–2.5±5.4	F7	2.1	0.36	–162.8±6.7	5955±144	–0.50±0.50	4.00±0.50	NM
55[d]	22:02:41	10:42:58	38	6.4±4.7	–2.5±4.7	K0	3.6	0.48	–67.4±2.1	5339±100	0.00±0.50	4.37±0.25	NM
56	22:02:44	10:41:31	35	–2.7±4.8	–7.5±5.2	K0	3.4	0.47	–38.7±5.0	5342±128	0.23±0.26	4.34±0.43	M
57	22:02:48	10:41:42	1151	0.6±2.5	2.3±2.9	B9	0.6	–0.05	–175.9±3.4	10727±316	–0.50±0.50	4.00±0.50	NM
58	22:02:56	10:41:51	58	23.9±1.7	–24.3±1.8	G5	2.1	0.40	1.6±2.6	5724±227	–0.42±0.19	3.80±0.30	M
59	22:02:44	10:42:12	50	4.8±3.5	–4.3±3.8	G5	–0.1	0.51	–14.5±4.5	5229±100	–0.39±0.28	3.04±0.39	NM
60[d]	22:02:42	10:42:38	35	–0.9±4.2	–11.1±4.2	G5	3.7	0.45	–112.9±3.7	5668±113	–0.61±0.21	4.37±0.33	NM
61	22:02:56	10:42:18	311	3.1±5.1	–31.0±5.5	A4	0.9	0.41	–336.2±7.2	5750±227	–2.00±0.50	3.31±0.37	NM
62	22:02:41	10:40:57	26	–4.1±4.5	–5.0±4.9	G5	2.2	0.46	–34.8±1.7	5452±209	–0.11±0.21	4.03±0.37	NM

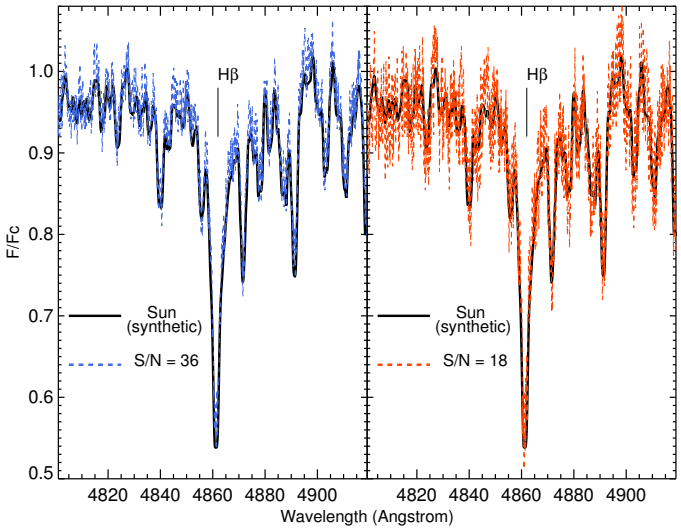

Fig. 5 PHOENIX synthetic spectrum representative of the Sun (*black lines*). Colored lines are the same spectrum, but degraded in S/N: S/N=36 (*left*) and S/N=18 (*right*). For better visualization, only the region around H_β is shown.

standards (HD 104471, HD 104982, HD 105004, CD-28 9374, HD 107122, HD 111433), previously observed (Maia 2012; Maia et al. 2009, hereafter MSCP09) with the same instrumental setup, and to six stars from the ELODIE library (HD 6920, HD 15866, HD 17382, HD 71497, HD 97633, HD 117176). Stars from these three samples were plotted with different symbols in Figure 7, where the present effective temperatures, surface gravities and metallicities were compared to the literature values. As explained above, the ELODIE library itself was used for the computation of $T_{\rm eff}$. For this reason, the six spectra obtained from it were not plotted in the leftmost part of Figure 7.

Although tested with only 15 objects, the derived parameters, computed as stated above, tend to reproduce the expected ones, taking into account the uncertainties. This demonstrates the usefulness of the synthetic library in the cross-correlation method, since it fills the gaps of the empirical library in the parameter space, especially for metallicities significantly different from the solar value. The better the parameter space resolution is, the higher the precision that is achieved in the stellar parameters derived.

Figure 8 shows the spectra of the standard stars HD 68089 and HD 211341 and of four science spectra (black lines). In each case, the PHOENIX model for which atmospheric parameters (red labels) are the closest to the measured ones was overplotted (red dotted lines). For reference, some prominent absorption lines were highlighted. The blue dots represent the residuals (science minus template) as a function of wavelength in each case. The horizontal continuous lines are the "zero" lines for the residuals.

Arbitrary constants were added to the spectra, which were corrected to the rest frame, for comparison purposes. Table 2 summarizes the results.

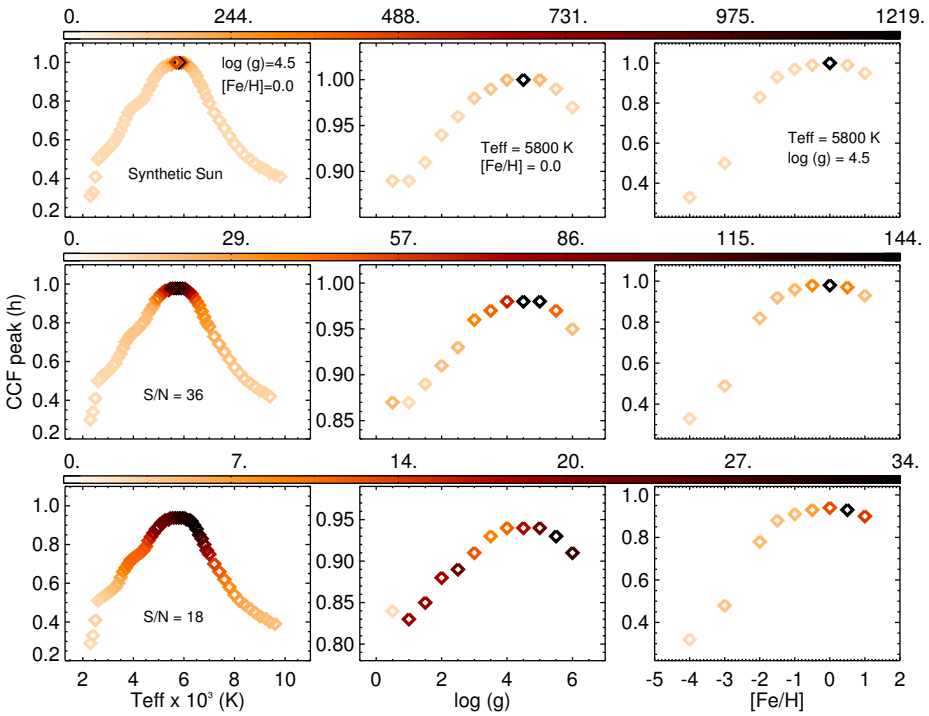

Fig. 6 Sensitivity of the cross-correlation function peaks (h) with respect to variations in $T_{\rm eff}$ (*leftmost column*), $\log(g)$ (*middle column*) and $[{\rm Fe/H}]$ (*rightmost column*). The upper panels show the results obtained with the original solar PHOENIX spectrum as the object. The *middle* and *lower* panels show the results obtained with the same solar spectrum, but degraded in S/N (see Fig. 5). The *top* plots on each column indicate the parameters that were kept fixed during the cross-correlation procedures. The color bars indicate the TDR values.

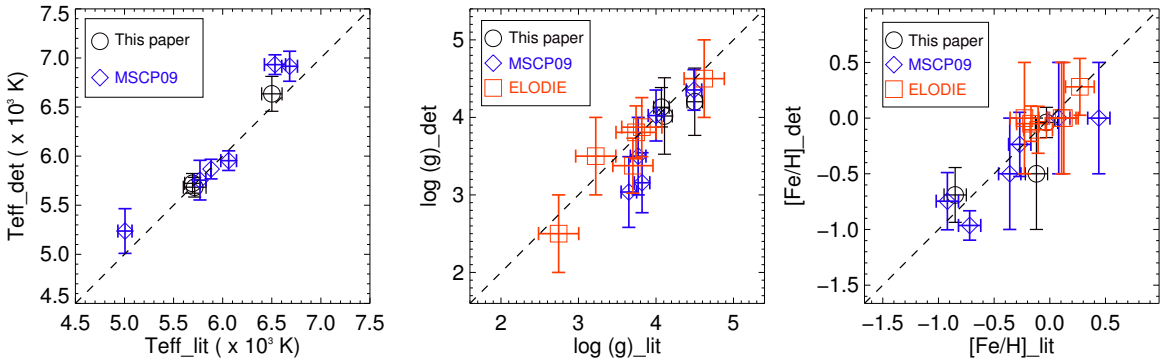

Fig. 7 Comparison between present and literature parameters ($T_{\rm eff}$, $\log(g)$ and $[{\rm Fe/H}]$) for a sample of fifteen stars. Spectra of three of them (HD 68089, HD 211341 and HD 38254) were reduced and analyzed for this paper. Six were previously observed and reduced (MSCP09) and another six were taken from the ELODIE library. The dashed line is the $y = x$ locus.

4 ANALYSIS

4.1 Photometric Analysis: Testing an OCR Nature

OCRs are intrinsically poorly populated (PKBM11). For this reason, it is useful to evaluate the statistical resemblance between the cluster and the field with respect to the sequences observed in CMDs. First, we built $K_s \times (J - K_s)$ CMDs for stars located in the inner area of NGC 7193 ($r \leq 10'$) and also for stars in an arbitrary control field, chosen in the region $30 \leq r$ (arcmin) ≤ 60 from a random ensemble of field samples with the same area as the central region. We then executed a routine that evaluates the overdensity of stars in the cluster CMD rel-

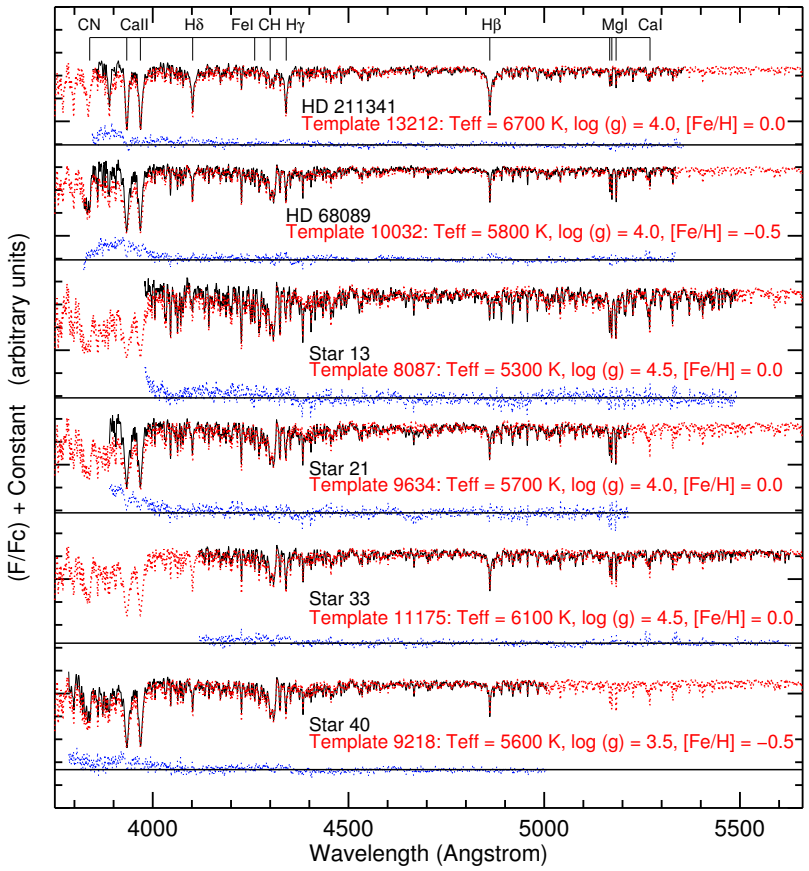

Fig. 8 Normalized and radial velocity corrected spectra of standard stars HD 68089 and HD 211341 and of four science spectra (*black lines*). In each case, the best-matched PHOENIX spectra are superimposed on the observed ones (*red dotted lines*). The blue dots represent the residuals (science minus template) as a function of wavelength in each case. The *horizontal continuous lines* are the "zero" lines for the residuals. Some deep absorption lines are marked for reference.

ative to the control field in order to establish photometric membership probabilities.

This algorithm (fully described in MSC10) builds 3D CMDs with J, $(J-H)$ and $(J-K_s)$ as axes for the cluster and control field. These diagrams are divided into small cells with sizes $(\Delta J, \Delta(J-H), \Delta(H-K_{\rm s}))$ that are proportional to the mean uncertainties in magnitudes and color indexes. In our case, cell sizes are 20 times the mean uncertainty in J and 10 times the mean uncertainties in $(J-H)$ and $(H-K_{\rm s})$. These cells are small enough to detect local variations of field-star contamination on the various sequences in the CMD, but are large enough to accommodate a significant number of stars (MSC10).

Membership probabilities are assigned to stars in each cell according to the relation $P = (N_{\rm clu} - N_{\rm con})/N_{\rm clu}$, where $N_{\rm clu}$ is the number of stars counted within a cell in the cluster CMD and $N_{\rm con}$ is the number counted in the corresponding cell in the control field CMD. Null probabilities are assigned whenever $N_{\rm clu} < N_{\rm con}$. The cell positions are changed by shifting the entire grid one-third of a cell size in each direction. The cell sizes are also increased and decreased by one-third of the average sizes in each of the CMD axes. Considering all of the possible configurations, 729 different grid sets are used. The final probability value for each star is derived by taking the average of the memberships obtained over the whole grid configurations. No star was removed from the cluster CMD.

In Figure 9, a PARSEC isochrone (Bressan et al. 2012) was superimposed on the cluster CMD with the fundamental parameters $(m-M)_0 = 8.5 \pm 0.2$ mag, $\log(t/{\rm yr}) = 9.4 \pm 0.2$, $E(B-V) = 0.05 \pm 0.05$ mag and $[{\rm Fe/H}] = -0.17 \pm 0.23$ (see Sect. 4.4 for details). The latter value (and its 1σ uncertainty) was obtained by averaging the metallicities estimated for the member stars, selected after our joint analysis (Sect. 4.4). The reddening value adopted in our analysis was obtained from

Schlegel et al. (1998) extinction maps and provides a decent fit to our data. It is consistent, within uncertainties, with that obtained from the maps of Green et al. (2015), from which we have $E(B-V) = 0.03 \pm 0.03$ mag. The dotted line represents the locus of unresolved binaries with equal-mass components. The blue and red dashed lines are Padova isochrones with $[\mathrm{Fe/H}] = -0.4$ and $[\mathrm{Fe/H}] = 0.06$, respectively, corresponding to the above lower and upper limits for $[\mathrm{Fe/H}]$. It is noticeable that the widening of the main sequence (MS) due to the metallicity uncertainty is much smaller than that caused by binaries. In order to properly select the isochrone, we used $[\mathrm{Fe/H}]$ as a proxy of the overall metallicity Z according to the relation: $[\mathrm{Fe/H}] = \log(Z/Z_{\odot})$, where $Z_{\odot} = 0.0152$ (Bressan et al. 2012). The color bar indicates the photometric membership probabilities, computed as explained above. The reddening correction was based on the extinction relations taken from Rieke & Lebofsky (1985): $A_J = 0.282A_V$, $A_H = 0.175A_V$ and $A_K = 0.112A_V$ with $A_V = 3.09E(B-V)$.

Following Pavani & Bica (2007, hereafter PB07) and PKBM11, an isochrone fitting index (n_{fit}) was defined as the number of stars, weighted by the membership probabilities, that are compatible with a given isochrone, taking into account photometric uncertainties. A star is considered to be a photometric member if it is at a maximum level of $3\sigma_{Ks}$ and $3\sigma_{(J-Ks)}$ from the nearest isochrone point. Formally

$$n_{\mathrm{fit}} = \sum_{j=1}^{N_{\mathrm{fit}}} P_j \qquad (1)$$

where P_j is the membership probability and N_{fit} is the number of cluster stars compatible with the isochrone. We took into account the effect of unresolved binaries by shifting the isochrone in steps of 0.01 mag in the direction of decreasing K_s up to 0.75 mag, which is the limit corresponding to unresolved binaries with equal mass (dotted line in Fig. 9). All stars compatible with these loci count in the sum given by Equation (1).

In general, contamination by field stars becomes more severe for fainter magnitudes in the cluster CMD, where photometric uncertainties are larger. For this reason, the calculation of n_{fit} (Eq. (1)) was restricted to stars with $K_s \leq 13$ mag and membership probabilities $P \geq 50\%$. Stars that obey these restrictions and that are compatible with the isochrone sequences (binaries included), plotted with error bars in Figure 9, yielded $n_{\mathrm{fit}} = 16.2$.

In the second step of our procedure, the same method stated above was applied to a set of 100 field regions randomly chosen around NGC 7193 ($30 \leq r$ (arcmin) ≤ 60). Arbitrary pairs of samples were taken within this ensemble and, for each pair, one of the samples was treated as a test field and the other one as a comparison field. The MSC10 algorithm was then executed to determine membership probabilities and to obtain n_{fit} for each test field−control field pair.

Figure 10 shows the resulting distribution of n_{fit} values. The cyan arrow indicates the value obtained for the OCR. The leftmost dashed line indicates the 90^{th} percentile of the distribution ($n_{\mathrm{fit}} = 10.5$), while the rightmost one indicates the 95^{th} percentile ($n_{\mathrm{fit}} = 12.4$). The n_{fit} value for the cluster is beyond the 95^{th} percentile of the distribution, which reveals a statistical contrast between the OCR and the field.

The value $n_{\mathrm{fit}} = 16.2$ was obtained with a particular choice for the control field. In the third step of our procedure, we compared the NGC 7193 $K_s \times (J-K_s)$ CMD with that of each one of the 100 randomly chosen field samples. For each cluster−control field pair, we determined n_{fit} using the procedure outlined above. The median of this set of values resulted in 11.3 (red arrow in Fig. 10), whose associated percentile is slightly greater than 90%. This result suggests that the sequences defined along the isochrone in the cluster CMD are statistically distinguishable from the field with a significance level of about 90%. The average value $\langle n_{\mathrm{fit,OCR}} \rangle$ obtained in this experiment resulted in $\langle n_{\mathrm{fit,OCR}} \rangle = 11.5 \pm 3.3$ (1σ). The possibility of a field fluctuation cannot be ruled out from the photometric analysis solely, since we have some field samples for which $n_{\mathrm{fit,field}} > n_{\mathrm{fit,OCR}}$ (Fig. 10). This is not an unexpected result, since we are dealing with a poor stellar aggregate that is barely distinguishable from field stars.

4.2 Kinematic Analysis

In this section, we perform a preselection of candidate member stars of NGC 7193 based on the spread of the variables' right ascension (α), declination (δ), radial velocity (V_{r}) and proper motion components ($\mu_\alpha \cos\delta$, μ_δ). The distribution of V_{r}, obtained via the procedure outlined in Section 3.2, is shown in Figure 11. The histogram bin (10 km s^{-1}) corresponds to twice the mean uncertainty in V_{r}. We identified five radial velocity groups: $V_{\mathrm{r}} \leq -200$, $-200 < V_{\mathrm{r}} \leq -100$, $-100 < V_{\mathrm{r}} \leq -50$, $-50 < V_{\mathrm{r}} \leq 10$ and $V_{\mathrm{r}} > 10$. Four stars with $V_{\mathrm{r}} < -120$ km s^{-1} seem to be unrelated to the other groups. The V_{r} values are shown in Table 2 together with all atmospheric parameters derived from our science spectra (Sect. 4.3). Proper motions were obtained from UCAC4.

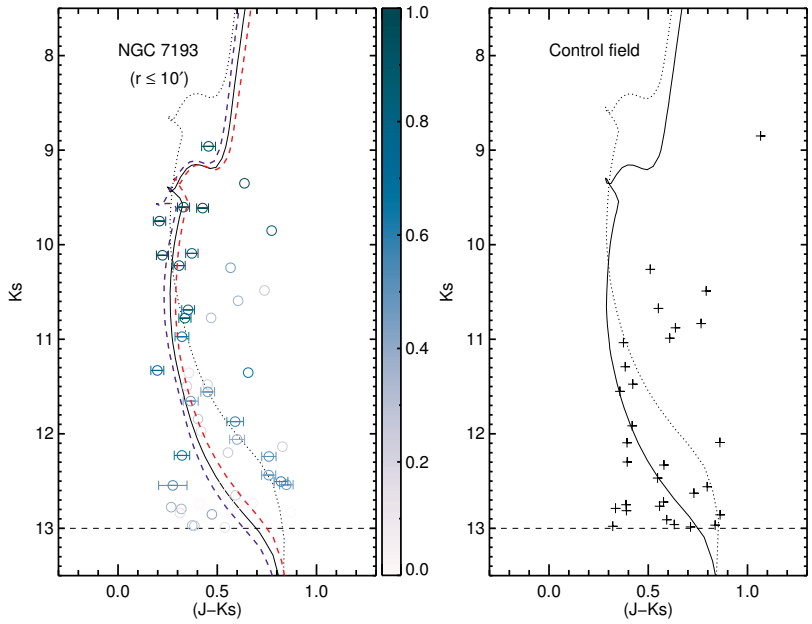

Fig. 9 *Left*: $K_s \times (J - K_s)$ CMD for NGC 7193. Only stars with $K_s \leq 13$ mag were plotted. The color bar indicates membership probabilities. A PARSEC isochrone ($\log(t/\mathrm{yr}) = 9.4$; $[\mathrm{Fe/H}] = -0.17$) was visually superimposed on the data. The *dotted line* represents the locus of unresolved binaries with equal-mass components. The *blue* and *red dashed lines* are Padova isochrones with $[\mathrm{Fe/H}] = -0.4$ and $[\mathrm{Fe/H}] = 0.06$, respectively (see text for details). Stars compatible with the isochrone (binaries included) and with $P \geq 50\%$ (see text) are plotted with error bars in $(J - K_s)$. *Right*: CMD for a control field (same area).

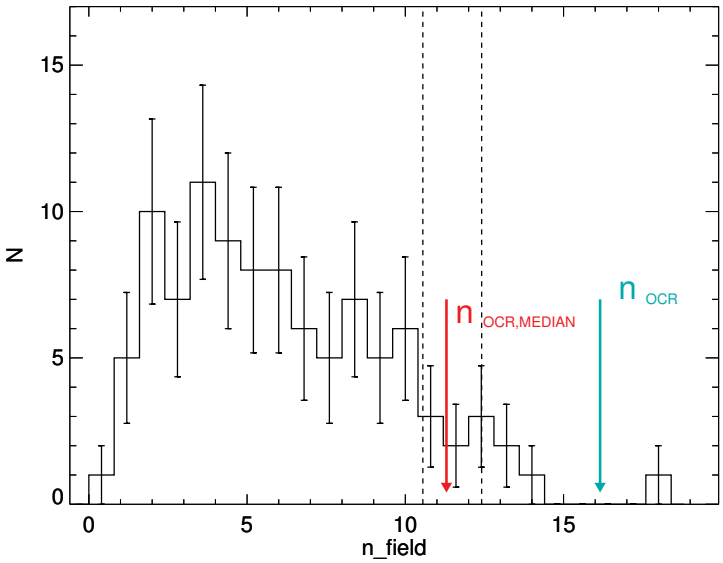

Fig. 10 Distribution of n_{fit} values (Eq. (1)) for the ensemble of field regions selected around NGC 7193. The *cyan arrow* indicates the value of n_{fit}, obtained for the cluster. The *red arrow* shows the median of n_{fit} values obtained after applying Equation (1) to data cluster−control field pairs. The *leftmost dashed line* indicates the 90^{th} percentile of the distribution, while the *rightmost* one corresponds to the 95^{th} percentile. Poisson error bars are shown.

A 5-dimensional iterative sigma-clipping routine, involving the kinematical and positional variables, was employed in order to identify a group of stars with motions compatible with each other and spatially localized in the cluster area. Francis & Anderson (2012, hereafter FA12) applied this method in order to find improved candidate lists for 87 clusters and associations from *The Extended Hipparcos compilation* ("XHIP", Anderson & Francis

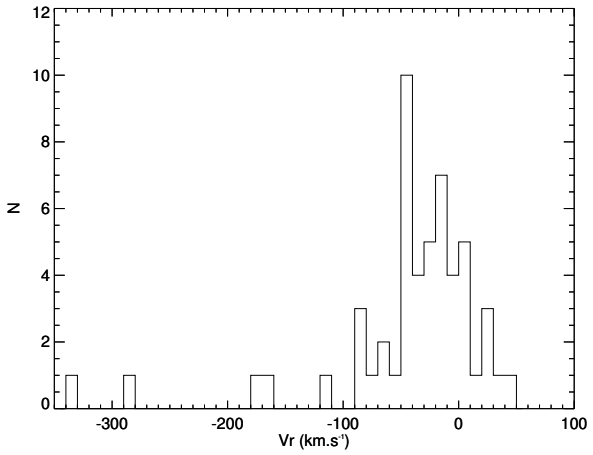

Fig. 11 Distribution of radial velocities derived from GMOS spectra.

2012). The algorithm consists of iteratively subjecting each star in our sample (Table 2) to the condition

$$\sum_{i=1}^{N} \frac{(X_i - \bar{X}_i)^2}{\sigma^2_{X_i}} < n^2 \qquad (2)$$

where, for a fixed exclusion criterion n, the summation runs over the variables $\{X_i\} = \{\alpha, \delta, V_{\rm r}, \mu_\alpha \cos\delta, \mu_\delta\}$. $\bar{X}_i$ and σ_{X_i} are, respectively, the mean and standard deviation for the group satisfying Equation (2) in the previous iteration.

At each iteration, all stars satisfying Equation (2) are included in a new subsample. The means and variances of each X_i are then recalculated. Stars that do not satisfy Equation (2) are excluded and another iteration is performed. The convergence criterion is simply that the number of candidate member stars does not change under subsequent iterations. For our data we adopted $n = 3.4$, which means that the algorithm excludes stars for which at least one of the X_i variables differs from $\bar{X}_i$ by more than 1.5 times the associated dispersion σ_{X_i}. This procedure resulted in a stable subsample with 43 stars (81% of the complete sample) after four iterations.

As stated by FA12, Equation (2) statistically defines the interior of a hyperellipsoid in the position $\times$ velocity space, centered at the mean for the cluster and with axes proportional to the standard deviation of each variable. The exclusion criterion generalizes to 5 dimensions the procedure of excluding data points that are beyond a given number of standard deviations from the sample mean.

Figure 12 shows the vector-point diagrams (VPDs) for stars in the inner area of NGC 7193 ($r \leq 10'$) and in a ring ($30 \leq r$ (arcmin) ≤ 31.6228) of the same area as that of the cluster, for comparison purposes. Stars observed spectroscopically were identified according to Table 2 and symbols correspond to different $V_{\rm r}$ bins. Blue symbols represent stars excluded after applying the FA12 algorithm (stars 51 and 53 are highly deviant and were not plotted for better readability) and red symbols represent those that were kept. Other stars are represented by small black circles. The mean uncertainties in $\mu_\alpha \times \cos\delta$ and μ_δ are indicated by error bars in Figure 12. The magnitude limits (16.5, 16.5 and 17.1 mag in J, H and K_s, respectively) for both plots correspond to the maximum magnitude values for stars in our spectroscopic sample (Table 2).

Non-excluded stars that are compatible with the isochrone sequences and binary loci on the cluster CMD (Sect. 4.4) form a preliminary list of member candidate stars. Ten stars (4, 23, 34, 44, 39, 51, 53, 54, 57 and 61) were excluded by the FA12 algorithm. As shown in Figure 12, these stars have very discrepant proper motion components (and/or radial velocities) compared to the bulk motion, taking into account the adopted exclusion criterion ($n = 3.4$ in Eq. (2)). Nevertheless, we cannot definitely rule out the membership of these stars because OCRs are dynamically evolved structures and thus they are expected to be rich in binaries (e.g., de la Fuente Marcos et al. 2013), in which the presence of a secondary appreciably changes the velocity of the primary star. This suggests that care must be taken when applying proper motion filters to sort out members. In addition, the VPDs for both NGC 7193 and the annular field show a close resemblance and we are not able to readily disentangle both populations based only on kinematic information. This is expected for a dissolving cluster since repeated encounters with external agents cause the mean motion of a cluster to be closer to the mean movement of the neighboring field (Maia 2012).

As stated by Bica & Bonatto (2005, hereafter BB05), it is useful to compare the proper motion distribution of stars in the cluster area with that of the control field stars in order to look for systematic deviations. Asymmetries and peaks in the intrinsic (i.e., field subtracted) proper motion distribution may yield information on the internal kinematics and presence of unresolved binaries (PB07).

Following the BB05 method, the proper motion distributions for NGC 7193 and for an annular field with the same area were constructed. Since UCAC4 also includes 2MASS photometry, the correspondence limit between both catalogs was firstly evaluated. The CMDs in Figure 13 show that both are nearly complete for $J \leq 14.5$ mag. Restricting our data to this limit is important to ensure that the proper motion distributions are not

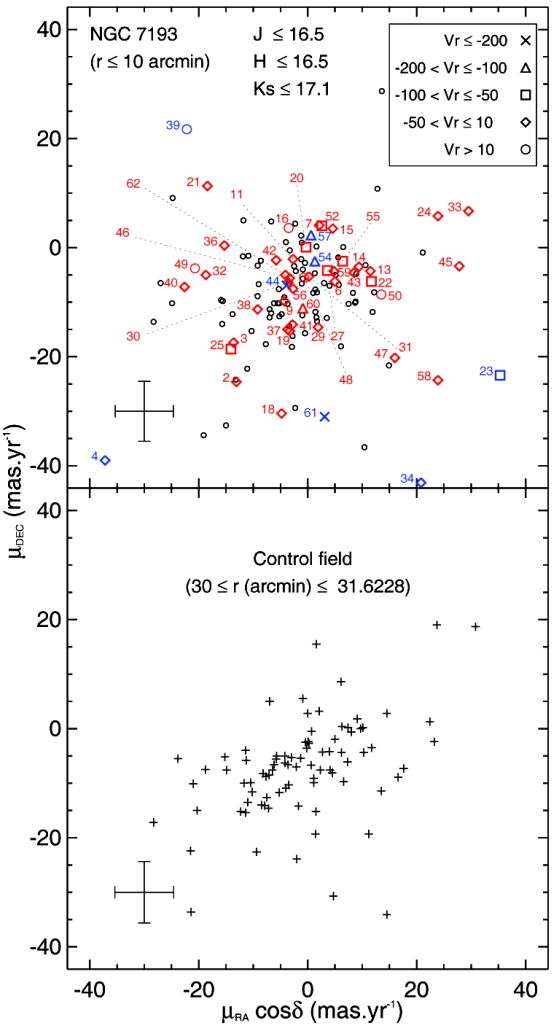

Fig. 12 *Top*: VPD for NGC 7193. Stars with spectroscopic data are numbered (see Table 2). Symbols refer to different radial velocity bins (in km s^{-1}). *Blue (red) symbols* refer to stars (not) excluded after applying the FA12 algorithm. *Small black circles* represent other stars in the target area. Magnitude limits are shown for both plots. *Bottom*: VPD for an annular field. Average error bars are plotted in both diagrams.

affected by incompleteness, especially for fainter magnitudes.

Besides this restriction in J, a color filter was applied to the photometric data of NGC 7193 and annular field (Sect. 4.4) in order to remove most of the background contamination, leaving a residual contribution that will be taken into account by means of histogram subtractions (PB07). Rather than working separately with proper motion components, the angular projected velocities on the sky ($V_{\rm p} = \sqrt{\mu_\alpha^2 \times \cos^2\delta + \mu_\delta^2}$) were employed in this study.

Figure 14 shows the distributions of $V_{\rm p}$ for NGC 7193 and the control field (left), and the field subtracted distribution (right). Histogram bins are 6 mas yr^{-1}, which is about 1$\times$ the average uncertainty in $V_{\rm p}$ for the sample of stars in Figure 14. The proper motion distribution for stars in NGC 7193 shows systematic deviations, taking Poisson uncertainties into account, with respect to the field distribution in the range $V_{\rm p} \leq 30$ mas yr^{-1} and a small overdensity in the range $42 \leq V_{\rm p}$ (mas yr^{-1}) ≤ 54. For a self-gravitating system, low-velocity peaks can be attributed to the internal spread of velocities for single stars, superimposed on the cluster's systemic motion. Higher-velocity peaks, in turn, may be produced by unresolved binaries (BB05).

Despite the presence of conspicuous peaks in the intrinsic $V_{\rm p}$ distribution, their reality is doubtful because of low number statistics, especially in the range between $42 - 54$ mas yr^{-1}. As stated previously, we are dealing with an object whose kinematics closely resembles that

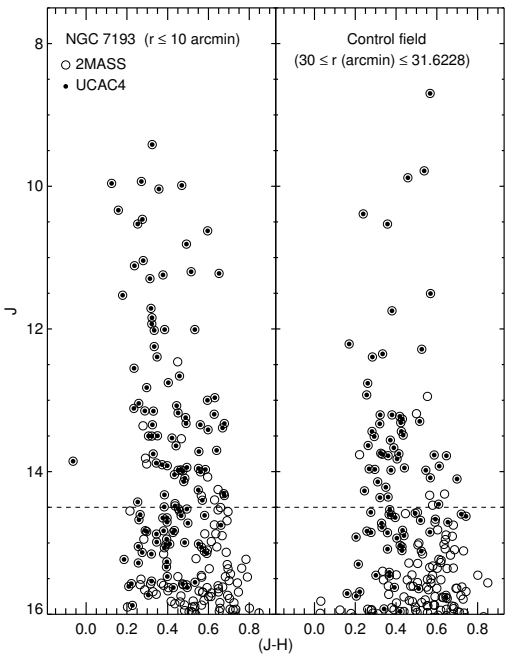

Fig. 13 Correspondence between 2MASS (*open circles*) and UCAC4 (*filled circles*) for NGC 7193 (*left*) and an annular field (*right*) with the same area. The correspondence limit between both catalogs is about 14.5 mag in J (*dashed line*).

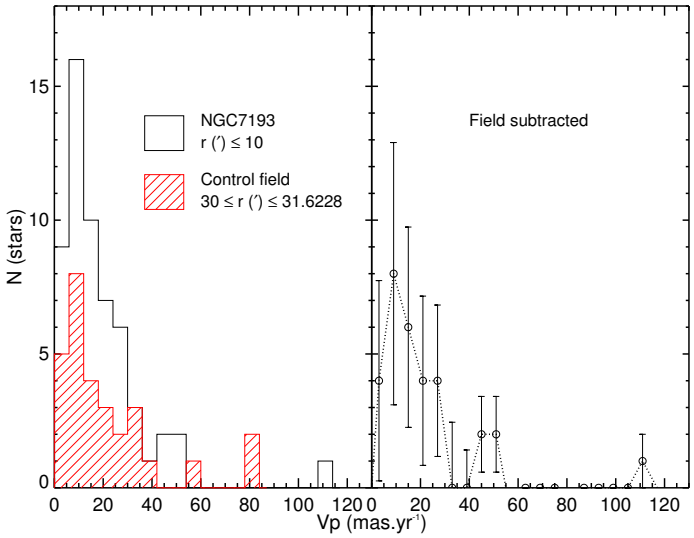

Fig. 14 *Left*: Distribution of angular projected velocities of stars in NGC 7193 (*empty histogram*) and in the annular field (*hatched histogram*). *Right*: Intrinsic proper motion distribution. Poisson error bars are overplotted.

of the field due to its physical nature. Thus we need more information, in addition to what is provided by kinematic data, in order to disentangle both populations.

4.3 Absolute Magnitudes and Intrinsic Colors for the Spectroscopic Sample

Following the procedures outlined in Section 3.2, atmospheric parameters and radial velocities were obtained for the 53 stars observed spectroscopically in the field of NGC 7193. The parameters are shown in Table 2 together with the proper motion components, obtained from UCAC4. To estimate absolute magnitudes and intrinsic color indexes, the position of each star in the temperature-gravity plane, which is independent of distance and reddening, was compared to PARSEC isochrones of the respective metallicity. Then, there were

selected model parameters that best fit the measured values and the corresponding absolute magnitude M_J and intrinsic color $(J-K_s)_0$ were taken. These are also presented in Table 2.

4.4 Joint Analysis: Cluster Membership

Photometric data in the near-infrared for stars in the inner ($r \leq 10'$) region of NGC 7193 and for a comparison field (external ring with the same area as the cluster) were extracted from 2MASS. In order to include all stars observed spectroscopically in the CMD analysis, the following magnitude limits were applied: 16.5, 16.5 and 17.1 mag for J, H and K_s, respectively. To improve the search for member candidates of NGC 7193, only those stars which have kinematic information in the UCAC4 catalog were considered.

Figure 15 shows the $K_s \times (J-K_s)$ CMDs for NGC 7193 and for a comparison field. NGC 7193 shows a contrasting overdensity of bright stars relative to the comparison field. Symbols, colors and identifiers for our spectroscopic sample follow those of Figure 12 (star 54 has a poor quality photometric flag in K_s and therefore was not plotted in Fig. 15).

We visually superimposed a PARSEC isochrone ($\log(t/\mathrm{yr}) = 9.4$, $[\mathrm{Fe/H}] = -0.17$) on the locus of data. The chosen isochrone was reddened by $E(B-V) = 0.05$ mag and vertically shifted to fit the observed magnitudes along the main sequence for determination of the distance modulus, which resulted in $(m-M)_0 = 8.5$ mag. Age was estimated by fitting the brightest stars close to the turnoff and subgiant branch. The corresponding fundamental parameters and their uncertainties are the same as those used in Section 4.1.

The dotted line in the CMDs of Figure 15 is a color filter applied to both cluster and comparison field data in order to remove most of the background contamination. The four green circles mark the stars (4, 23, 34 and the one with $K_s = 13.341$ and $(J-K_s) = 0.662$) whose projected angular velocities V_p are in the range $42-54$ mas yr^{-1} and that produce the overdensity in this interval of V_p in Figure 14.

The dot-dashed line is the MS of Koornneef (1983) shifted by the distance modulus with reddening derived from isochrone fitting. K and $(J-K)$ values were transformed into 2MASS magnitudes and colors according to Carpenter (2001) relations.

As stated in Section 4.2, we built a preliminary list of member candidate stars by selecting those that were *not* excluded after applying the FA12 algorithm (red symbols in Figs. 12 and 15) and that are compatible with the isochrone (binaries included) within a maximum level of $3\sigma_{K_s}$ and $3\sigma_{(J-K_s)}$ (same fitting criterion adopted in Section 4.1). This subsample is composed of stars 3, 6, 9, 11, 13, 14, 16, 21, 29, 31, 33, 37, 38, 40, 41, 42, 45, 48, 49, 56, 58 and 60. Although star 55 is close to the lower MS, it does not have uncertainty in K_s according to 2MASS and a poor quality photometric flag is attributed to it. Therefore, this star was excluded from our subsample. The average and 1σ dis-

Table 3 Data for Member Candidate Stars based on Photometry and Proper Motions (uncertainties are in parentheses)

ID	α_{2000} (h: m: s)	δ_{2000} ($^\circ$: $'$: $''$)	$\mu_\alpha \cos\delta$ (mas yr^{-1})	μ_δ (mas yr^{-1})	Memb. (**)
89	22:03:07	10:49:39	–15.9	–9.6	PM
			(6.9)	(5.6)	
98	22:03:20	10:51:42	–1.2	2.2	PM
			(4.4)	(4.8)	
102	22:03:16	10:43:31	4.0	–7.0	LPM
			(8.4)	(7.5)	
108	22:03:13	10:42:30	1.4	–11.8	PM
			(4.4)	(4.8)	
112	22:03:14	10:54:11	–5.3	–7.6	LPM
			(4.5)	(4.9)	
117	22:03:34	10:46:32	–0.5	–2.8	PM
			(4.6)	(5.0)	
122	22:02:46	10:44:10	–13.8	–12.2	PM
			(8.3)	(7.9)	
125	22:03:23	10:53:54	1.7	–8.2	LPM
			(4.4)	(4.8)	
131	22:03:16	10:55:09	1.6	0.2	PM
			(2.2)	(2.8)	
132	22:03:36	10:50:39	–5.2	–10.2	PM
			(4.1)	(4.6)	
133	22:03:28	10:42:30	1.3	–4.7	PM
			(18.9)	(18.7)	
136	22:03:29	10:42:31	–11.1	–22.2	PM
			(2.8)	(3.3)	
140	22:02:36	10:47:25	–3.3	–0.5	PM
			(6.9)	(6.5)	
142	22:03:33	10:53:36	–24.9	–10.2	PM
			(4.2)	(4.6)	
144	22:02:35	10:47:04	12.2	–8.2	LPM
			(4.3)	(4.9)	
146	22:03:29	10:54:37	8.9	–4.8	PM
			(4.2)	(4.7)	
147	22:02:46	10:54:22	–11.8	5.0	PM
			(5.6)	(5.4)	
161	22:02:30	10:46:39	6.5	0.1	PM
			(4.1)	(4.5)	
162	22:02:43	10:55:35	–7.0	–11.3	PM
			(4.8)	(5.2)	

Notes: ** PM means a probable member and LPM means a less probable member star.

persion of proper motion components for this set of 22 stars resulted in $\langle \mu_\alpha \cos\delta \rangle = -0.11 \pm 14$ mas yr^{-1} and $\langle \mu_\delta \rangle = -6.7 \pm 8.0$ mas yr^{-1}. The large dispersion of these values can be ascribed both to the limited accuracy of the proper motion data and to the presence of unresolved binaries that remained after applying the FA12 algorithm (Sect. 4.2).

In order to include possible members without observed spectra, we selected a group of stars that are compatible with the isochrone and the binary loci, and whose proper motion components are compatible with the above means, within 2σ, for $\mu_\alpha \cos\delta$ and μ_δ. Nineteen stars satisfy these restrictions and are represented in Figure 15 as filled symbols in the following K_s intervals: $11.25 < K_s \leq 12.4$ (big circles), $12.4 < K_s \leq 13$ (squares), $13 < K_s \leq 13.7$ (triangles) and $K_s > 13.7$ (small circles). Data for these member candidate stars are shown in Table 3. For better legibility, these stars were not labeled in the CMD. Non-member stars are plotted as small open circles.

The 22 stars listed above, for which there are spectroscopic data, together with the other 19 member candidates, selected based on photometry and proper motions but without spectra, were plotted in the intrinsic $(J-H)_0 \times (H-K_s)_0$ color-color diagram (CCD) shown in Figure 16. Symbols and identifiers are the same as those in Figures 12 and 15. Intrinsic color sequences for dwarfs and giants from Straižys & Lazauskaitė (2009) were overplotted. The star colors were dereddened by $E(B-V) = 0.05$. For better visualization, error bars were overplotted only on stars with available spectra and for which the colors uncertainties are smaller than or equal to 0.1 mag. For stars 11, 16, 48 and 60, average errors in $(J-H)$ and $(H-K_s)$ are 0.13 mag and 0.18 mag, respectively. For the 19 member candidate stars without available spectra, average errors are 0.05 mag and 0.06 mag in $(J-H)$ and $(H-K_s)$, respectively. Although excluded by the FA12 algorithm (Sect. 4.2), stars 4, 34, 44 and 53 were also plotted in the CCD, since they are compatible with the isochrone sequences or the binary loci shown in the NGC 7193 CMD (Fig. 15).

4.4.1 Final list of members

In order to refine our list of cluster members, a star-by-star analysis was performed to identify stars for which spectral types (see Table 2) are compatible with their expected positions on the CCD, taking photometric uncertainties and reddening vector into account. A group of stars with compatible positions within both CMD and CCD was thus selected. After determining individual distances via spectroscopic parallax (using the photometric information for each star), additional constraints were established: we selected a group of stars whose metallicities are compatible with each other within uncertainties and whose mean distance is compatible with that obtained by isochrone fitting.

Among our spectroscopic sample, the list of members is composed of 15 stars: 3, 6, 13, 14, 21, 31, 33, 34, 40, 41, 45, 49, 53, 56 and 58. The average distance and 1σ dispersion for this group of stars resulted in $\langle d \rangle = 548 \pm 250$ pc, which is compatible with the distance value obtained from the CMD analysis (501 ± 46 pc) within uncertainties. Taking into account the latter heliocentric distance and the Galactocentric distance (R_G) of the Sun (8.00 ± 0.50 kpc, Reid 1993), the value of R_G for NGC 7193 resulted in 7.87 ± 0.50 kpc, which places it in the solar circle. The average metallicity for this group resulted in $\langle [\mathrm{Fe/H}] \rangle = -0.17 \pm 0.23$ ($Z \approx 0.010$).

Stars 34 and 53 were excluded by the FA12 algorithm, since their proper motion components are highly discrepant from the bulk motion (Fig. 12) and their positions in the NGC 7193 CMD suggest that both objects are likely binary systems. We took proper motion data from the list of the remaining 13 spectroscopic members together with the 19 probable members (Tables 2 and 3, respectively) of NGC 7193 and obtained the cluster dispersion of projected velocities (σ_{Vp}). The 3D velocity dispersion (σ_v) was obtained from σ_{Vp} assuming isotropy. With this approximation, $\sigma_v = \sqrt{3/2} \times \sigma_{Vp}$. With this procedure, the result for NGC 7193 was $\sigma_v = 25.6 \pm 2.7$ km s^{-1}. If we restrict this sample to those stars that have radial velocity information, the dispersion of their composite velocities ($V = \sqrt{V_\mathrm{r}^2 + (\mu_\alpha \times \cos\delta)^2 + \mu_\delta^2}$) results in $\sigma_v = 20.9 \pm 1.7$ km s^{-1}, a value that is nearly compatible with that obtained from the isotropic approach. In this step, we transformed proper motions (pm) into linear velocities using the distance modulus $(m-M)_0 = 8.5$ mag and the relation

$$v(\mathrm{km\ s^{-1}}) = pm\,(\mathrm{mas\ yr^{-1}}) \times d\,(pc) \times 4.74 \times 10^{-3}.$$

The high velocity dispersions obtained for NGC 7193 are comparable to the one obtained by PB07 for a group of OCRs (see their fig. 12, where the dispersion in V_p for their group B is about 30 km s^{-1}). This may be a consequence of the highly evolved dynamical state of the OCRs. In this context, de la Fuente Marcos et al. (2013) analyzed the case of the OCR NGC 1252. After a proper selection of member candidate stars (their section 5), they obtained a dispersion value of 3.0 mas yr^{-1} for proper motion in RA

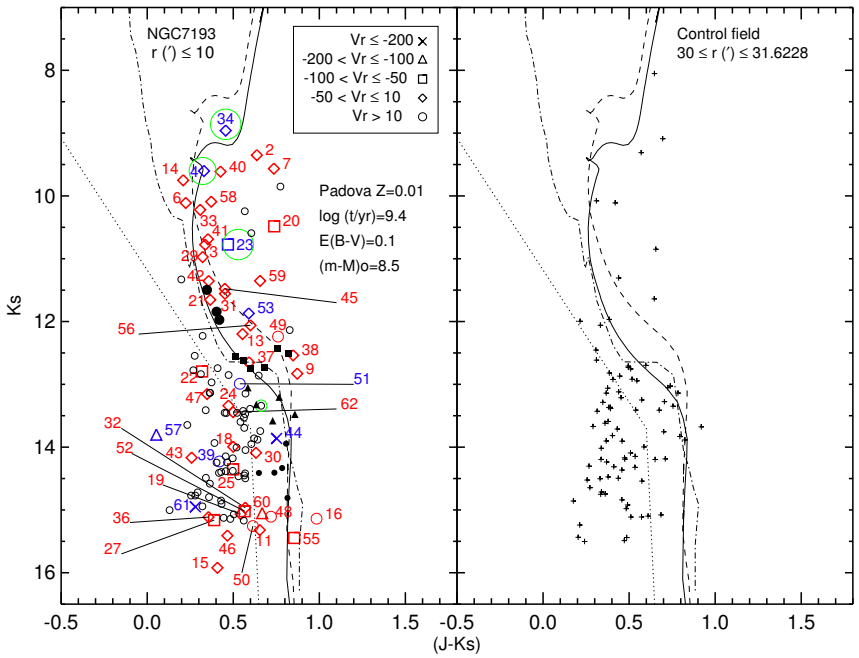

Fig. 15 *Left*: $K_s \times (J-K_s)$ CMD for NGC 7193. Symbols, colors and identifiers follow Fig. 12. A PARSEC isochrone (*continuous line*) was superimposed on the data (basic parameters are shown). The *dashed line* represents the locus of unresolved binaries with equal-mass components. The *dotted line* represents the color filter. The *dot-dashed line* is the MS of Koornneef (1983) shifted by the derived distance modulus and reddened. The *four green circles* mark the stars that produce the overdensity in the range $42 \leq V_{\rm p}$ (mas yr^{-1})≤ 54 in Figure 14. Filled symbols (*big circles*: $11.25 < K_s \leq 12.4$; *squares*: $12.4 < K_s \leq 13$; *triangles*: $13 < K_s \leq 13.7$; *small circles*: $K_s > 13.7$) are possible member stars without spectroscopic data (see text for details). *Small open circles* are non-member stars. *Right*: same as left, but for a comparison field.

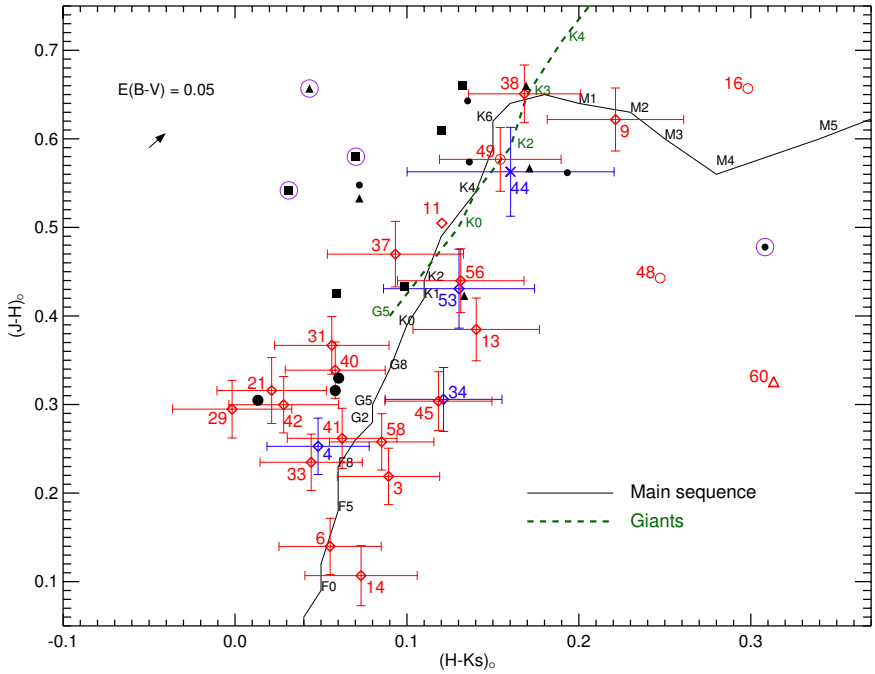

Fig. 16 Intrinsic CCD for NGC 7193. A de-reddening correction of $E(B-V) = 0.05$ was applied to each star. Colors, symbols and identifiers are the same as those used in Figs. 12 and 15, except for the *purple circles*, which identify four stars considered less probable members (see text for details). Sequences from Straižys & Lazauskaitė (2009) for dwarfs and giants are overplotted. Some spectral types are indicated, for reference.

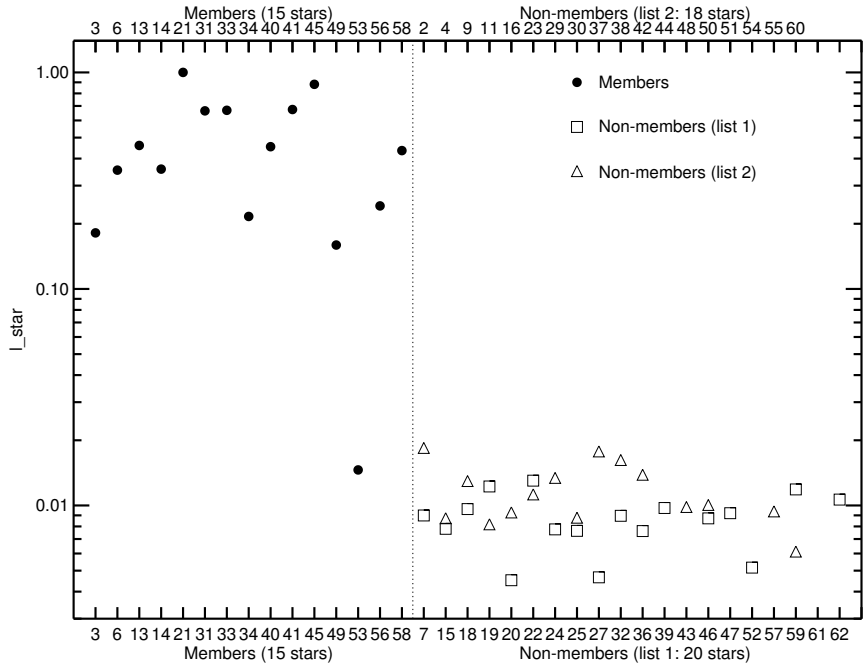

Fig. 17 Normalized individual likelihoods calculated (Eq. (3)) for the group of member and non-member stars. The latter group was divided into two subsamples; stars 43, 44, 51, 54, 57 and 61, which have normalized likelihoods smaller than 0.003, were not plotted, for visualization purposes.

and 2.8 mas yr^{-1} for the dispersion of proper motion in DEC. The resulting dispersion in the projected velocities is $\sigma_{Vp} = \sqrt{\sigma^2_{\mu_\alpha \times \cos\delta} + \sigma^2_{\mu_\delta}} = 4.10$ mas yr^{-1}. For an assumed distance of 1.1 kpc, this translates into $\sigma_{Vp} = 21.4$ km s^{-1}. In the isotropic approximation, the 3D velocity dispersion is $\sigma_v = \sqrt{3/2} \times \sigma_{Vp} = 26.2$ km s^{-1}, for an estimated mass of $12 \pm 5\ M_\odot$ (our estimation, for which we have employed the list of member candidates present in table 4 of de la Fuente Marcos et al.'s paper). As a consequence of the dynamical evolution, the total binary fraction within the cluster is expected to increase with time (de La Fuente Marcos 1998).

Only stars 21 and 33 seem to be displaced from their expected position on the CCD, taking into account the spectral types determined for them. However, Figure 8 shows similarity between their spectra and the corresponding synthetic ones, suggesting that the technique employed has provided good matches and that their atmospheric parameters are well determined. The discrepancies may be attributed to uncertainties in $T_{\rm eff}$ and/or to inaccuracy in the spectral classification of the best ELODIE templates used for $T_{\rm eff}$ determination (Sect. 3.2).

Among the possible member stars without available spectra (filled symbols in the NGC 7193 CMD and CCD), those with $(J-H)_0 < 0.43$ (six stars) are compatible with the intrinsic sequences in Figure 16 considering photometric uncertainties. Their spread along these sequences is similar to that verified for the member stars observed spectroscopically. The same comment can be stated for those stars with $0.52 < (J-H)_0 < 0.66$ and $0.11 < (H-K_s)_0 < 0.19$ (seven stars). Among stars within the ranges $(J-H)_0 > 0.5$ and $(H-K_s)_0 < 0.07$ (five stars), three of them (marked with purple circles) are incompatible with the sequences in the CCD, even taking uncertainties into account. These were considered less probable member stars, as well as the one with $(J-H)_0 = 0.463$ and $(H-K_s)_0 = 0.300$.

Membership flags have been assigned to stars in Table 2, which were observed spectroscopically, and also for those in Table 3, which were considered member candidates based on photometry and proper motions. "M" means a *member*, "PM" means a *probable member*, "LPM" means a *less probable member* and "NM" means a *non-member* star. Our final list of NGC 7193 members contains 34 stars: 15 of them are labeled as "M" in Table 2 and the other 19 stars are presented in Table 3 (labeled as "PM" or "LPM").

To check that our final list of members is statistically distinguishable from field stars, we carried out Kolmogorov-Smirnov (K-S) two-sample tests comparing

the values of $V_{\rm r}$, [Fe/H] and $V_{\rm p}$ for the group of member stars and the group of non-member stars. In each case we verified the statistical similarity between these two samples of stars observed spectroscopically. These comparisons indicated that the probability for non-member stars being representative of the member group, in terms of the distributions of $V_{\rm r}$, [Fe/H] and $V_{\rm p}$, is 5.1%, 4.4% and 6.6%, respectively. This result reveals a significant separation between these two samples when the parameters are taken into account separately.

In order to deepen our analysis, we also performed statistical comparisons taking into account the three parameters together with the photometric information. We followed a procedure analogous to that adopted by Dias et al. (2012) in order to establish membership probabilities for star clusters in general. For each star in the sample, a membership likelihood ($l_{\rm star}$) is computed in a four-dimensional space. The likelihood includes $V_{\rm r}$, [Fe/H], $V_{\rm p}$ and the distance of each star to the nearest isochrone point computed according to Section 4.1. Mathematically, the likelihood for a given star is expressed as

$$
\begin{aligned}
l_{\rm star} = & \frac{1}{\sigma_{V_{\rm r}}\sigma_{\rm [Fe/H]}\sigma_{V_{\rm p}}\sigma_{\rm dist}}\times \\
& \exp -\frac{1}{2}\left[\left(\frac{V_{\rm r,star}-\langle V_{\rm r}\rangle}{\sigma_{V_{\rm r}}}\right)^2\right]\times \\
& \exp -\frac{1}{2}\left[\left(\frac{\rm [Fe/H]_{star}-\langle [Fe/H]\rangle}{\sigma_{\rm [Fe/H]}}\right)^2\right]\times \\
& \exp -\frac{1}{2}\left[\left(\frac{V_{\rm p,star}-\langle V_{\rm p}\rangle}{\sigma_{V_{\rm p}}}\right)^2\right]\times \\
& \exp -\frac{1}{2}\left[\left(\frac{\rm dist_{star}-\langle dist\rangle}{\sigma_{\rm dist}}\right)^2\right]\times
\end{aligned}
\qquad (3)
$$

where $\sigma_{V_{\rm r}}$, $\sigma_{\rm [Fe/H]}$, $\sigma_{V_{\rm p}}$ and $\sigma_{\rm dist}$ are calculated via a quadrature sum of the individual errors with the final dispersion of each parameter for the sample of member stars; $\langle V_{\rm r}\rangle$, $\langle$[Fe/H]$\rangle$, $\langle V_{\rm p}\rangle$ and $\langle$dist$\rangle$ are the mean values of each parameter for the group of members; $V_{\rm r,star}$, $\rm [Fe/H]_{star}$, $V_{\rm p,star}$ and $\rm dist_{star}$ are the values of each parameter for a given star. Consequently, this a posteriori calculation takes into account these four parameters simultaneously (calculated multiplicatively as shown in Eq. (3)) and provides a combined membership probability.

The same calculation was performed for the group of non-member stars, keeping the dispersions as defined above; that is, relative to the mean values for the group of members.

Figure 17 shows the ensemble of normalized likelihoods, where we can see a clear distinction between members and non-members.

NGC 7193 may be the remnant of a once very populous OC. From the simulations of Baumgardt & Makino (2003) for clusters in an external tidal field, Lamers et al. (2005) establish an approximate scaling between dissolution time ($t_{\rm dis}$) of a cluster and initial number of stars (N_0): $t_{\rm dis} \propto N^{0.65}$, in the range $\sim 10^3 - 10^6\ M_\odot$. Based on this scaling, the initial stellar content of NGC 7193 may have been as rich as $N_0 \sim 10^4$ stars. This result is in agreement with de La Fuente Marcos (1998), whose simulations with an initial population of $\sim 10^4$ stars are able to reproduce observable quantities of evolved open clusters (his figure 2).

5 LUMINOSITY AND MASS FUNCTIONS

Photometric data for the member stars were employed to build the luminosity function (LF) of NGC 7193 by counting the number of stars in magnitude bins of $\Delta K_s = 0.72$ mag, as shown in Figure 18. Representative MS spectral types (taken from Straižys & Lazauskaitė 2009) are shown in addition to Poisson error bars. The turnoff (TO) magnitude is also indicated.

For comparison purposes, the initial MF of Kroupa (2001, hereafter K01) was converted to LF (red line in Fig. 18) by using a PARSEC isochrone ($\log(t/{\rm yr}) = 9.4$, [Fe/H] $= -0.17$, as derived in Sect. 4.4) and its mass-luminosity relation. Mathematically, $\Phi_L(K_s) \propto m^{-\alpha}|\frac{dm}{dK_s}|$, where α is the slope of the initial MF. K01 MF was scaled to match the total present MS mass of NGC 7193 (see below) and absolute magnitudes were converted to apparent ones by applying the distance modulus and reddening derived from isochrone fitting. The K01 MF wiggle at $K_{\rm s} \simeq 14.2$ (Fig. 18) is produced by the change of slope at $0.5\ M_\odot$, from $\alpha = 2.3$ to 1.3, as the mass decreases.

Noticeable depletion of low-mass MS stars can be verified in Figure 18 for spectral types later than ∼K0 ($m \lesssim 0.8\ M_\odot$). This result should not be attributed to photometric incompleteness of the UCAC4 catalog, since only the last histogram bin is formed solely by stars with $J > 15$ mag and thus fainter than the correspondence limit ($J = 14.5$ mag) between 2MASS and UCAC4 (see Fig. 13). This depletion can be interpreted as a consequence of the preferential loss of lower mass stars by evaporation, which is a signature of dynamically evolved OCs (de La Fuente Marcos 1997 and Portegies Zwart et al. 2001).

The LF shown in Figure 18 was then restricted to stars along the MS and converted to MF. Again, we

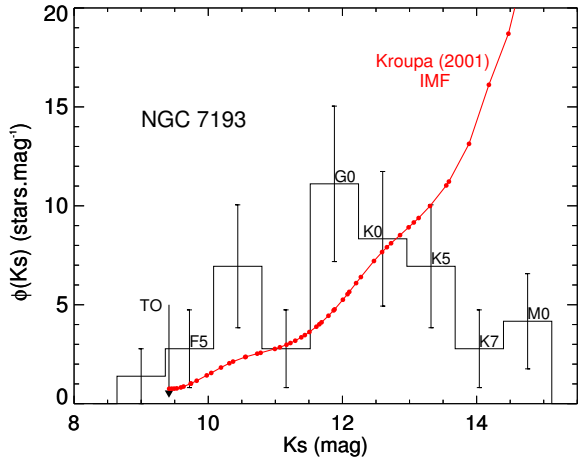

Fig. 18 LF $\Phi_L(K_s)$ for NGC 7193 in terms of apparent magnitude K_s. The TO and some MS representative spectral types are shown. Poisson error bars are overplotted. For comparison, the initial MF of K01 was converted to LF (*red continuous line*), as detailed in the text.

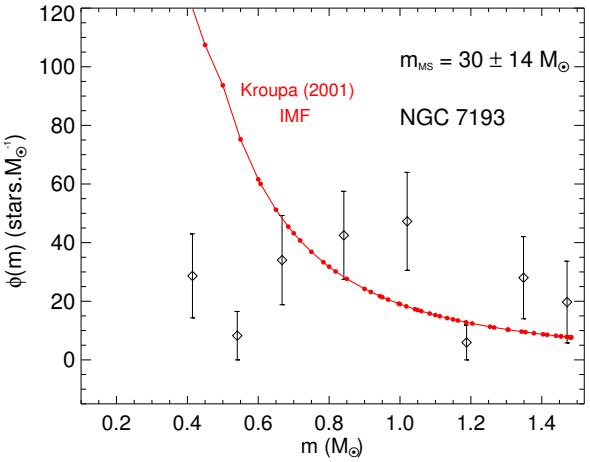

Fig. 19 MF $\Phi(m)$ for NGC 7193 MS stars. Uncertainties come from error propagation. The *red line* shows the K01 initial MF, for comparison.

used the stellar mass-luminosity relation from the selected PARSEC isochrone. The NGC 7193 MF is shown in Figure 19 together with the K01 MF. The considerable variations in the cluster MF and the huge errors do not allow a statistically significant fit to the data. Consequently, the present observed MS stellar mass in NGC 7193 has been estimated by numerically integrating its MF. The resulting observed stellar mass is $m_{\rm MS} = 30 \pm 14\ M_\odot$. Star 34 is the only member with $K_s < K_{s,\rm TO}$. Its mass was assumed as the mass of the nearest isochrone point: $m_{34} \approx 1.5\ M_\odot$. Thus, the total estimated mass for NGC 7193 is $32 \pm 14\ M_\odot$.

6 SUMMARY AND CONCLUDING REMARKS

Due to its physical nature, NGC 7193 bears resemblance to the field, as can be noted by comparing the VPDs for both target and control field (Fig. 12) and their CMDs (Fig. 15). A visual inspection of both plots reveals that we are not able to readily disentangle both populations based only on one kind of data.

Despite this, there is evidence to support the idea of NGC 7193 being a coeval stellar aggregate. Star counts in the cluster's inner area show an overdensity compared to the field for $R_{\rm lim} = 10'$ (Fig. 4). This overdensity is also evident in the cluster RDP (Fig. 2). This significant contrast with respect to the field is the first step towards establishing a possible physical nature (BSDD01).

We tested the physical nature of NGC 7193 based only on photometric information in Section 4.1. By counting the number of stars compatible with the isochrone sequences (binaries included), taking membership probabilities into account (Fig. 9), we defined an isochrone fitting index (Eq. (1)) and evaluated $n_{\rm fit}$ for stars in the cluster's inner area. This value was then compared with the distribution of $n_{\rm fit}$ values obtained for an ensemble of field regions randomly chosen (Fig. 10). This experiment demonstrated that the sequences defined along the isochrone in the cluster CMD are distinguishable from the field with a significance level of about 90%.

We compared the distribution of angular projected velocities of stars in NGC 7193 and in a control field (Fig. 14), after restricting proper motion data to stars with $J \leq 14.5$ mag (Fig. 13) and applying a color filter (Fig. 15) to the data in both regions, in order to remove most of the background contamination. The intrinsic (i.e., field subtracted) distribution of angular projected velocities (Fig. 14, right) shows some residual peaks, despite the large Poisson error bars, which is a consequence of low number statistics. This result is consistent with the presence of a self-gravitating system, for which low-velocity peaks in the intrinsic distribution may be attributed to the internal spread of velocities of single stars, superimposed on the systemic motion of the cluster, and higher-velocity peaks may be produced by unresolved binaries (BB05).

Based on the data for stars observed spectroscopically (Table 2), we applied the FA12 algorithm (Sect. 4.2) in order to identify a group of stars with motions compatible with each other and spatially localized in the cluster area. Ten of 53 stars were iteratively excluded (blue symbols in Fig. 12) after applying the criterion defined by Equation (2). Among the non-excluded stars (red symbols in Figure 12), we built a preliminary list of mem-

ber stars by selecting those that are compatible with the isochrone in the CMD of Figure 15. Nineteen probable member stars without spectroscopic information, but which had compatible proper motions and also photometric data consistent with the isochrone sequences, were selected (Table 3).

The preliminary list of members was plotted in the intrinsic $(J-H)_0 \times (H-K_s)_0$ CCD (Fig. 16). We added to this subsample of stars that was excluded by the FA12 algorithm but which are consistent with the isochrone sequences, since these may be binary systems. In order to refine our list of members, we performed a star-by-star analysis to identify stars whose spectral types are coherent with their expected positions on the CCD, taking photometric uncertainties and reddening into account. Additional constraints were established by selecting a group of stars whose metallicities are compatible with each other within uncertainties and for which the mean distance is compatible with that obtained by isochrone fitting. Our final list of members is composed of those stars labeled as 'M' in the last column of Table 2 together with those member candidate stars shown in Table 3 (labeled as 'PM' or 'LPM'). Finally, photometric data for these stars were employed to build the luminosity function and MF of NGC 7193 and its total mass was estimated (Sect. 5).

Our results present large discrepancies compared to those of Tadross (2011). After extracting 2MASS data for stars in the NGC 7193 area ($r \leq 7'$) and in a nearby control field, he employed a decontamination algorithm that counts the number of stars within a given magnitude and color range in the control field CMD and subtracts this number from the cluster CMD. This is performed for a grid of cells with fixed sizes. A solar-metallicity Padova isochrone (Bonatto et al. 2004a) was then fitted to the data in the field-subtracted CMD. His results were (his table 3): $t = 4.5 \pm 0.18$ Gyr, $d = 1080 \pm 50$ pc and $E(B-V) = 0.03 \pm 0.01$. Our results, in turn, for the same parameters are: $t = 2.5 \pm 1.2$ Gyr, $d = 501 \pm 46$ pc and $E(B-V) = 0.05 \pm 0.05$. These discrepancies can be attributed to the different criteria adopted for the selection of member candidate stars. We advocate that a proper characterization procedure applied to an object with such low number statistics should contain not only photometric information, but also spectroscopic and proper motion data. The dispersions of the derived parameters and the spread of data along recognizable sequences in both CMD and CCD should be jointly verified to probe the physical connection between stars.

In this paper we have developed a fruitful technique to analyze poorly-populated stellar systems and applied it to the OCR candidate NGC 7193. This method allowed us to investigate its physical nature by means of the coherence obtained for the properties of 15 stars. We statistically compared the sample of members and non-members using K-S tests and a likelihood expression and concluded that both samples are essentially different, confirming that NGC 7193 is a genuine OCR.

We conclude that NGC 7193 is a 2.5 Gyr OCR composed of 15 confirmed members and 19 probable members and located about 500 pc away from the Sun. Its resulting limiting radius, mass, mean metallicity and Galactocentric distance are $R_{\rm lim} = 1.5 \pm 0.1$ pc, $M = 32 \pm 14\ M_\odot$, $\langle [{\rm Fe/H}] \rangle = -0.17 \pm 0.23$ and $R_G = 7.87 \pm 0.50$ kpc respectively. The luminosity and mass functions of NGC 7193 show a depletion of low-mass stars. This suggests a preferential loss of lower mass stars by evaporation, which is a signature of dynamically evolved objects. Furthermore, there is evidence that NGC 7193 may be the remnant of a once very populous OC ($N_0 \sim 10^4$ stars).

In a forthcoming paper, we will apply the method described in this paper to a larger sample of similar objects in order to achieve more assertive statements about the general properties of these challenging systems and thus to provide better observational constraints for evolutionary models. The study of OCRs is a subject of great interest, since they are important for our understanding of the formation and early evolution of the Galactic disc.

Acknowledgements The authors are grateful to the anonymous referee for helpful comments. We thank the Brazilian financial agencies FAPEMIG (grant APQ-01858-12) and CNPq. We also thank the Gemini staff/resident astronomers for their support and service during observations. This publication makes use of data products from the Two Micron All Sky Survey, which is a joint project of the University of Massachusetts and the Infrared Processing and Analysis Center/California Institute of Technology, funded by the National Aeronautics and Space Administration and the National Science Foundation. This research has made use of the WEBDA database, operated at the Institute for Astronomy of the University of Vienna, and of the SIMBAD database, operated at CDS, Strasbourg, France. This research has made use of Aladin and data from the UCAC4 and PPMXL catalogs.

References

Anderson, E., & Francis, C. 2012, Astronomy Letters, 38, 331
Baumgardt, H., & Makino, J. 2003, MNRAS, 340, 227
Bica, E., & Bonatto, C. 2005, A&A, 431, 943 (BB05)

Bica, E., Santiago, B. X., Dutra, C. M., et al. 2001, A&A, 366, 827 (BSDD01)
Bonatto, C., Bica, E., & Girardi, L. 2004a, A&A, 415, 571
Bonatto, C., Bica, E., & Pavani, D. B. 2004b, A&A, 427, 485
Bressan, A., Marigo, P., Girardi, L., et al. 2012, MNRAS, 427, 127
Carpenter, J. M. 2001, AJ, 121, 2851
Carraro, G., de La Fuente Marcos, R., Villanova, S., et al. 2007, A&A, 466, 931
Casagrande, L., Schönrich, R., Asplund, M., et al. 2011, A&A, 530, A138
Ciddor, P. E. 1996, Appl. Opt., 35, 1566
de La Fuente Marcos, R. 1996, A&A, 314, 453
de La Fuente Marcos, R. 1997, A&A, 322, 764
de La Fuente Marcos, R. 1998, A&A, 333, L27
de la Fuente Marcos, R., de la Fuente Marcos, C., Moni Bidin, C., Carraro, G., & Costa, E. 2013, MNRAS, 434, 194
Dias, W. S., Alessi, B. S., Moitinho, A., & Lépine, J. R. D. 2002, A&A, 389, 871 (DAML02)
Dias, W. S., Monteiro, H., Caetano, T. C., & Oliveira, A. F. 2012, A&A, 539, A125
Francis, C., & Anderson, E. 2012, Astronomy Letters, 38, 681 (FA12)
Green, G. M., Schlafly, E. F., Finkbeiner, D. P., et al. 2015, ApJ, 810, 25
Holmberg, J., Nordström, B., & Andersen, J. 2009, A&A, 501, 941
Husser, T.-O., Wende-von Berg, S., Dreizler, S., et al. 2013, A&A, 553, A6
King, I. 1962, AJ, 67, 471
Koornneef, J. 1983, A&A, 128, 84
Kroupa, P. 2001, MNRAS, 322, 231 (K01)
Lamers, H. J. G. L. M., Gieles, M., Bastian, N., et al. 2005, A&A, 441, 117
Maia, F. F. S. 2012, Caracterização e evolução estrutural de aglomerados abertos da Galáxia, PhD thesis, Universidade Federal de Minas Gerais, Belo Horizonte, MG
Maia, F. F. S., Corradi, W. J. B., & Santos, Jr., J. F. C. 2010, MNRAS, 407, 1875 (MSC10)
Maia, F. F. S., Santos, Jr., J. F. C., Corradi, W. J. B., & Piatti, A. E. 2009, Boletin de la Asociacion Argentina de Astronomia La Plata Argentina, 52, 109 (MSCP09)
Moultaka, J., Ilovaisky, S. A., Prugniel, P., & Soubiran, C. 2004, PASP, 116, 693
Pavani, D. B., & Bica, E. 2007, A&A, 468, 139 (PB07)
Pavani, D. B., Bica, E., Ahumada, A. V., & Clariá, J. J. 2003, A&A, 399, 113
Pavani, D. B., Bica, E., Dutra, C. M., et al. 2001, A&A, 374, 554
Pavani, D. B., Kerber, L. O., Bica, E., & Maciel, W. J. 2011, MNRAS, 412, 1611 (PKBM11)
Portegies Zwart, S. F., McMillan, S. L. W., & Gieles, M. 2010, ARA&A, 48, 431
Portegies Zwart, S. F., McMillan, S. L. W., Hut, P., & Makino, J. 2001, MNRAS, 321, 199
Reid, M. J. 1993, ARA&A, 31, 345
Rieke, G. H., & Lebofsky, M. J. 1985, ApJ, 288, 618
Roeser, S., Demleitner, M., & Schilbach, E. 2010, AJ, 139, 2440
Schlegel, D. J., Finkbeiner, D. P., & Davis, M. 1998, ApJ, 500, 525
Schmidt-Kaler, Th., 1982, in Landolt-Bornstein New Serires Vol. 2b: Astron- omy and Astrophysics/Star and Star clusters 14 (Springer-Verlag Newbak)
Skrutskie, M. F., Cutri, R. M., Stiening, R., et al. 2006, AJ, 131, 1163
Straižys, V., & Lazauskaitė, R. 2009, Baltic Astronomy, 18, 19
Tadross, A. L. 2011, Journal of Korean Astronomical Society, 44, 1
Tonry, J., & Davis, M. 1979, AJ, 84, 1511 (TD79)
Villanova, S., Carraro, G., de la Fuente Marcos, R., & Stagni, R. 2004, A&A, 428, 67
Zacharias, N., Finch, C. T., Girard, T. M., et al. 2013, AJ, 145, 44